Elemental abundances in M31: [Fe/H] and [α/Fe] in M31 Dwarf Galaxies Using Coadded Spectra

Jennifer Wojno,[1] Karoline M. Gilbert,[1,2] Evan N. Kirby,[3] Ivanna Escala,[3,4] Rachael L. Beaton,[4,5,*]
Erik J. Tollerud,[2] Steven R. Majewski,[6] and Puragra Guhathakurta[7]

[1]*Department of Physics and Astronomy, Johns Hopkins University, 3400 N. Charles St, Baltimore, MD 21218, USA*
[2]*Space Telescope Science Institute, 3700 San Martin Dr., Baltimore, MD 21218, USA*
[3]*California Institute of Technology, 1200 E. California Blvd., MC 249-17, Pasadena, CA 91125, USA*
[4]*Department of Astrophysical Sciences, Princeton University, 4 Ivy Lane, Princeton, NJ 08544*
[5]*The Observatories of the Carnegie Institution for Science, 813 Santa Barbara St., Pasadena, CA 91101*
[6]*Department of Astronomy, University of Virginia, Charlottesville, VA 22904-4325, USA*
[7]*Department of Astronomy & Astrophysics, University of California, Santa Cruz, 1156 High Street, Santa Cruz, CA 95064, USA*

ABSTRACT

We present chemical abundances of red giant branch (RGB) stars in the dwarf spheroidal (dSph) satellite system of Andromeda (M31), using spectral synthesis of medium resolution (R ∼ 6000) spectra obtained with the Keck II telescope and DEIMOS spectrograph via the Spectroscopic and Photometric Landscape of Andromeda's Stellar Halo (SPLASH) survey. We coadd stars according to their similarity in photometric metallicity or effective temperature to obtain a signal-to-noise ratio (S/N) high enough to measure average [Fe/H] and [α/Fe] abundances. We validate our method using high S/N spectra of RGB stars in Milky Way globular clusters as well as deep observations for a subset of the M31 dSphs in our sample. For this set of validation coadds, we compare the weighted average abundance of the individual stars with the abundance determined from the coadd. We present individual and coadded measurements of [Fe/H] and [α/Fe] for stars in ten M31 dSphs, including the first [α/Fe] measurements for And IX, XIV, XV, and XVIII. These fainter, less massive dSphs show declining [α/Fe] relative to [Fe/H], implying an extended star formation history. In addition, these dSphs also follow the same mass-metallicity relation found in other Local Group satellites. The conclusions we infer from coadded spectra agree with those from previous measurements in brighter M31 dSphs with individual abundance measurements, as well as conclusions from photometric studies. These abundances greatly increase the number of spectroscopic measurements of the chemical composition of M31's less massive dwarf satellites, which are crucial to understanding their star formation history and interaction with the M31 system.

Keywords: galaxy: M31 — galaxies: dwarf — galaxies: abundances

1. INTRODUCTION

Deriving detailed chemical abundances of stars is a crucial component in modeling the history of galaxies. Chemical abundance patterns across stellar populations provide information for both external (e.g. halo accretion/merger history; Bullock & Johnston 2005; Cooper et al. 2010; Font et al. 2011), as well as internal (e.g. radial migration; Gilmore et al. 2002; Boeche et al. 2013;

Corresponding author: Jennifer Wojno
jwojno1@jhu.edu

* Hubble Fellow
  Carnegie-Princeton Fellow

Kordopatis et al. 2015; Hayden et al. 2015) evolutionary processes. The ratio of α elements to iron (Fe) is especially illuminating with respect to a galaxy's star formation history. This is because α-elements and iron-peak elements are produced on distinctly different timescales, and can therefore act as an indicator for the star formation history in a particular environment (Tinsley 1979; Gilmore & Wyse 1991, 1998). α elements, such as oxygen and magnesium, are produced predominantly by one source: core-collapse supernovae. The progenitors of these supernovae are massive (M > 8$M_\odot$), and have well-known lifespans (∼ 10^6 years, Arnett 1996; Pagel 1997; Woosley & Janka 2005). In comparison, iron-peak elements are produced primarily in Type Ia supernovae

(Tinsley 1980) on significantly longer timescales ($\gtrsim 10^8$ years, Smecker-Hane & Wyse 1992; Nomoto et al. 1997; Matteucci 2001; Ishigaki et al. 2012). Stars with higher [α/Fe] ratios formed from gas enriched by core-collapse supernovae, while stars with lower [α/Fe] ratios formed from gas with a higher iron content – after Type Ia SNe released their ejecta into the ISM. In this way, the ratio of [α/Fe] and trends in [α/Fe]–[Fe/H] space provide clues to disentangle the enrichment timescale of a given population, the environment in which it formed, and its initial mass function.

Before the era of large-scale, ground-based spectroscopic surveys, such abundance measurements have been limited to stars within the Milky Way (MW), or MW satellites. It is now possible to push beyond the boundaries of our own Galaxy, and determine spectroscopic metallicities for red giant stars in our nearest neighbour, Andromeda (M31) (see Escala et al. 2019a,b; Gilbert et al. 2019, for the most recent such studies). At a distance of 760 kpc (Tully et al. 2013), the Andromeda galaxy is the closest grand-design spiral galaxy to the MW, and provides an opportunity to study in detail the formation history of a massive galaxy external to our own. Distinguishing the difference in the chemical evolution, in particular [α/Fe], between these galaxies is crucial in addressing a number of open questions relating to differences in the accretion history of their respective halos (e.g. Ibata et al. 1994, 2001; Carollo et al. 2007; Ibata et al. 2013; Helmi et al. 2017), their star formation history, the differences their morphology (e.g. bulge-to-disk ratios), and exploring the universality of [α/Fe] trends in massive galaxies.

Vargas et al. (2014a) produced the first individual metallicity and abundance ([Fe/H] and [α/Fe]) measurements of stars in nine M31 satellites. Their sample consisted of red giant branch (RGB) stars in M31 dwarf spheroidal (dSph) satellites, observed with the Deep Imaging Multi-Object Spectrometer (DEIMOS; Faber et al. 2003) instrument on Keck II, using the medium-resolution ($R \sim 6000$) 1200 l mm^{-1} (1200G) grating, covering the wavelength region 6300 Å $< \lambda < 9100$ Å. To derive individual abundance measurements, they used a spectral synthesis method first described by Kirby et al. (2008), and further developed by Vargas et al. (2013), where observed spectra are compared to a grid of synthetic spectra. Across their sample of nine M31 satellites, they found a large range of average [α/Fe], with no correlation between [α/Fe] and internal kinematics, stellar density, or proximity to M31.

To investigate the abundance distribution of the M31 halo, Vargas et al. (2014b) identified a sample of four stars in M31 dSph fields that were highly likely to belong to the M31 halo. They compared the abundance pattern of their stars to those in the Milky Way halo and found rough agreement between the M31 outer halo and the MW halo. More recently, Escala et al. (2019b, hereafter E19) expanded on this sample, producing individual abundance measurements for eleven stars in the M31 halo, located at 23 projected kpc from the center of M31. This sample was obtained using DEIMOS's 600 l mm^{-1} (600ZD) grating, which offers the advantage of larger wavelength coverage (4500 Å $< \lambda < 9000$ Å), as well as increased signal-to-noise (S/N) per pixel compared to the 1200G grating for a given exposure time.

Using the same abundance pipeline, Escala et al. (2019a) measured [Fe/H] and [α/Fe] in four additional M31 fields: the smooth outer halo, inner halo, the Giant Stellar Stream (GSS) and its kinematically cold substructure, and the outer disk. Their final sample, consisting of 70 RGB stars across all four fields, was used to illustrate differences in the accretion histories between the inner and outer halo components, as well as the effect of a major merger on the star formation rate in the disk of M31. Gilbert et al. (2019) focused on the GSS, and presented [Fe/H] measurements for 61 stars, with [α/Fe] measurements for 21 of these. They compared their abundance measurements to M31 dSphs, investigating the progenitor mass of the GSS. Finally, Kirby et al. (2020) presented [Fe/H] and [α/Fe] for 256 RGB stars in five M31 dSphs: And I, And III, And V, And VII, and And X. They compare their abundance measurements with MW dwarf satellites, as well as the smooth halo of M31 and the GSS.

As made clear from previous papers in this series (Escala et al. 2019a,b; Gilbert et al. 2019; Kirby et al. 2020), significant progress is being made in determining individual abundances for stars in M31 and its satellite galaxies. However, sample sizes are not yet large enough to provide maximally informative constraints on the star formation history of M31. Obtaining high enough S/N to measure [Fe/H] and [α/Fe] for individual stars requires a significant time investment. At the distance of M31, using a 10-m class telescope such as Keck, obtaining high enough S/N for RGB spectra to determine chemical abundances requires on the order of a few hours exposure time. As a result, a large majority of the spectra gathered for individual stars is below the threshold of signal to noise required to measure chemical abundances for individual stars.

However, Yang et al. (2013) explored the possibility of coadding similar spectra to obtain average chemical abundances ([Fe/H], [α/Fe]). They tested a coaddition procedure using RGB stars in MW globular clusters (GCs) and dwarf spheroidal galaxies (dSphs), using

1200 l mm^{-1} DEIMOS spectra. For stars with high enough S/N to obtain individual measurements, they compared the results of their pipeline to other high quality measurements in the literature, finding good agreement. They also compared the inverse-weighted average [Fe/H] and [α/Fe] to the results from coadded stars. They proposed that this method can be extended to measure average [Fe/H] and [α/Fe] from coadded spectra in M31, primarily using spectra that do not have the S/N needed to measure chemical abundances.

In this study, we extend the measurement of [Fe/H] and [α/Fe] abundances through spectral synthesis to coadded spectra in M31. We update the pipeline described in Yang et al. (2013) by implementing it in Python, and take into account additional fit uncertainties that result from adopting photometric stellar parameters in the spectral synthesis. The majority of large scale spectroscopic surveys in M31 so far have been focused on obtaining radial velocity measurements to study the kinematics of substructure in the halo, the internal velocity dispersions of M31 satellites, and the dynamics of the M31 disk (Tollerud et al. 2012, 2013; Collins et al. 2011, 2013; Gilbert et al. 2018). The Spectroscopic and Photometric Landscape of Andromeda's Stellar Halo (SPLASH, Guhathakurta et al. 2005, 2006; Gilbert et al. 2006) survey has collected tens of thousands of RGB spectra throughout the M31 halo, disk, and its satellites (e.g., Kalirai et al. 2010; Dorman et al. 2012, 2015; Gilbert et al. 2012, 2014; Tollerud et al. 2012). Many of these spectra do not have the S/N needed to determine metallicity and abundances for individual stars, and are therefore the perfect candidates for coaddition.

This paper is organized as follows. In Section 2, we describe the observation and instrument configurations used to gather the data used in our analysis. Section 3 gives a brief outline of the chemical abundance pipeline used to determine individual [Fe/H] and [α/Fe] measurements for RGB stars. Section 4 describes the selection criteria for our sample of stars to be coadded, as well as changes made to this pipeline to handle coadded spectra. In this section we also describe the coaddition process. In Section 5, we show results for validation tests used to verify that our coaddition method produces similar results to the weighted average abundance for a group of spectra, and how we determine the overall uncertainties on our coadded abundance measurements. In Section 6, we present results from our coaddition pipeline using spectra for which individual abundance measurements had large uncertainties, and compare them to our sample of validation coadds. We present the 2D [α/Fe]-[Fe/H] distribution in Section 7, and discuss the impli-

cations of our findings in the larger context of the star formation history of M31 and its satellites. Finally, Section 8 summarizes our results, and describes potential future applications of our coaddition process.

2. OBSERVATIONS AND PRIMARY DATA REDUCTION

We use spectra of red giant stars in six Milky Way globular clusters (average S/N across the whole sample of 158.13 per angstrom, Kirby et al. 2008, 2010, 2016), and ten M31 satellite galaxies observed as part of the SPLASH survey (Tollerud et al. 2012; Gilbert et al. 2012, 2018), obtained using the DEIMOS instrument (Faber et al. 2003) on Keck II.

2.1. *Target Selection*

The method for selecting candidate RGB stars in M31 is described in detail in Gilbert et al. (2006), Guhathakurta et al. (2006), Kalirai et al. (2006), and Tollerud et al. (2012). Shallow ($\sim 1-2$ hr) observations were obtained first (see Table 1), where stars likely to be RGB stars at the distance of M31 based on their CMD position were given the highest preference during the slitmask design process. The target selection for the deep (~ 6 hr exposure) masks was further refined using the shallow spectra to preferentially select stars highly likely to be M31 dSph members. Additional details regarding the design of the shallow masks can be found in Kalirai et al. (2009, 2010) and Tollerud et al. (2012). The imaging used for target selection for the shallow masks targeting And I, II, III, V, VII, IX, and XIV was obtained using the Washington M and T_2 filters, as well as the DDO51 intermediate filter (Ostheimer 2003; Kalirai et al. 2006; Tollerud et al. 2012; Beaton 2014). And X was discovered using photometry from the Sloan Digital Sky Survey (SDSS) (Adelman-McCarthy et al. 2006), and masks were designed using data from Zucker et al. (2007). Target selection for And XV was done using Canada-France-Hawaii Telescope archival imaging (Tollerud et al. 2012). The mask for And XVIII was designed using B and V-band imaging from the Large Binocular Telescope (LBT) (Beaton 2014).

For the slitmasks with deep observations, the photometry used to design the slitmasks was obtained from observations conducted with the Mosaic camera on the Kitt Peak National Observatory (KPNO) 4-meter telescope (Beaton 2014; Kirby et al. 2020). Imaging was obtained in the Washington M and T_2 bands. The photometric transformations relations from Majewski et al. (2000) were used to transform photometry from the Washington M and T_2 magnitudes to Johnson-Cousins V and I. A star's position in (I, V - I) color-magnitude space was then used as part of the criteria

to identify M31 RGB stars from MW field stars (see Section 4.1). In addition, photometry was obtained using the intermediate-width, surface-gravity sensitive DDO51 filter. Objects were assigned a DDO51 parameter, corresponding to the likelihood of the object being an RGB star, based on its position in (M - DDO51) - (M - T_2) color-color space (Palma et al. 2003). In general, objects with point-like morphology and high values of the DDO51 parameter were given the highest priority when constructing the spectroscopic slit masks for DEIMOS.

2.2. *Observations*

For five of these galaxies (And I, III, V, VII, and X), we have deep ($\sim$ 6 hour total exposure time, $\langle$S/N$\rangle$ = 15.3 per angstrom) spectroscopic observations. For all ten M31 dSphs, we have shallow spectroscopic observations ($\sim$ 1 − 2 hour total exposure time, $\langle$S/N$\rangle$ = 7.6 per angstrom). We note that these shallow masks were originally designed for obtaining kinematic information only, while the deep masks were explicitly designed to get high enough S/N to determine abundances for individual stars. Details of the observations for each slit-mask can be found in Table 1.

Spectra were obtained using the 1200G (1200 l mm^{-1}) grating, with the OG550 order blocking filter. The observed spectra cover a spectral range of $\sim$ 6300Å $< \lambda <$ 9100Å, with a resolution of $\sim$ 6000 at the central wavelength of $\sim$ 7800Å. The spectral dispersion of this science configuration is 0.33Å pix^{-1}, with a resolution of 1.2 Å FWHM.

2.3. *Data reduction pipeline*

One-dimensional science spectra were extracted from raw 2D DEIMOS spectra using the DEEP2 DEIMOS data reduction pipeline, contained within the spec2d IRAF package, developed by the DEEP2 Galaxy Redshift Survey[1] (Cooper et al. 2012; Newman et al. 2013). Details on modifications made for better performance on bright stellar sources (versus faint galaxies for which the pipeline was written) can be found in Simon & Geha (2007). Line-of-sight velocities for each star were obtained by cross-correlating observed spectra with the stellar templates provided in Simon & Geha (2007). To correct for the imperfect centering of a star in the slit, we use the relative positions of the Fraunhofer A band and other telluric absorption features (Simon & Geha 2007; Sohn et al. 2007).

3. INDIVIDUAL ABUNDANCE MEASUREMENTS

To determine spectroscopic effective temperature, [Fe/H], and [α/Fe] for individual stars, we adopt the synthetic spectral synthesis method outlined in Kirby et al. (2008), and further refined in Escala et al. (2019b) using a Python-based implementation of the method. An in-depth comparison between the results from the two pipelines (Kirby et al. (2008), written in IDL, and Escala et al. (2019b), written in Python) is provided in Appendix A. The observed spectrum is compared to a grid of synthetic spectra, and the [Fe/H] and [α/Fe] values from the best fit synthetic spectrum are adopted as our measured value. We apply this method to all individual spectra in our MW GC and M31 dSph samples, regardless of their S/N, or any other quality criteria (see Section 4.1).

3.1. *Photometric atmospheric stellar parameters*

Photometric effective temperature ($T_{\rm eff,phot}$), surface gravity (log g), and photometric metallicity ([Fe/H]$_{\rm phot}$) for individual stars are determined by linearly interpolating between isochrones, assuming a single distance for a given object. Assuming an age of 14 Gyr and [α/Fe] = +0.3 dex, we find the best-fit Padova (Girardi 2016), Victoria-Regina (VandenBerg et al. 2006), and Yonsei-Yale (Demarque et al. 2004) isochrones, using a star's position in ($I, V − I$) space. We take the error-weighted mean of all three isochrone sets as our final measured $T_{\rm eff,phot}$, log g, and [Fe/H]$_{\rm phot}$. While there are slight variations between the photometric values derived from the different isochrone sets, they do not significantly affect the abundance measurement (Kirby et al. 2008). Additionally, we justify a single age and α-enhancement by noting that for our sample, $T_{\rm eff,phot}$ and log g are largely insensitive to variations in age and assumed [α/Fe] of the isochrone set. For individual stars, $T_{\rm eff,phot}$ is used as a first approximation in measuring spectroscopic $T_{\rm eff}$, and log g is held constant throughout the spectroscopic abundance fitting procedure.

3.2. *Synthetic spectral grid*

The construction of the grid of synthetic spectra for the 1200G grating is described in detail in Kirby et al. (2008, 2009) and Kirby (2011). To summarize, synthetic spectra are generated using modified ATLAS9 model atmospheres (Kirby 2011; Kurucz 1993; Sbordone et al. 2004; Sbordone 2005) without convective overshooting (Castelli et al. 1997). The line list for atomic transitions were sourced from the Vienna Atomic Line Database (VALD; Kupka et al. 1999), molecular lines from Kurucz (1992), and the hyperfine transition line list from Kurucz (1993), where the oscillator strengths were tweaked to match values from observed spectra of the Sun and Arcturus (Kirby 2011). The parameter ranges for the stellar

---

[1] http://deep.ps.uci.edu/spec2d/

Table 1. MW globular cluster and M31 satellite observations obtained with the 1200G grating on Keck II/DEIMOS.

Object name	Mask name	Date	Airmass	$t_{\exp}$ (s)	$N_{members}$
MW GCs[a]					
NGC 2419	n2419c	2009 Oct 13	1.18	4800	54
NGC 6656 (M22)	n6656b	2009 Oct 13	1.48	4020	47
NGC 1904 (M79)	1904l2	2014 Aug 28	2.37	4200	18
NGC 6341 (M92)	n6341b	2011 Jun 2	1.1	1800	26
NGC 6864 (M75)	6864aB	2011 Aug 5	1.34	4800	39
NGC 7078 (M15)	7078l1B	2014 Aug 28	1.02	3600	41
M31 dSphs					
Deep observations[b,c]					
And I	and1a	2016 Dec 29	...	18300	26
And III	and3a	2016 Sep 7	...	19059	26
And V	and5a	2016 Sep 27	...	24275	49
	and5b	2016 Dec 29	...	17981	45
And VII	and7a	2017 Jan 1	...	16503	74
And X	and10a	2016 Sep 28	...	17760	12
	and10b	2017 Jan 1	...	22165	10
Shallow observations					
And I	d1_1	2005 Nov 05	1.07	4055	17
	d1_2	2005 Sep 16	1.49	3600	22
And II	d2_1	2005 Sep 06	1.36	3600	51
	d2_2	2005 Sep 06	1.13	3600	36
And III	d3_1	2005 Sep 08	1.56	3600	27
	d3_2	2005 Sep 08	1.22	3600	16
	d3_3	2009 Aug 23	1.05	3600	10
And V	d5_1	2008 Sep 30	1.13	3000	29
	d5_2	2008 Sep 30	1.27	2250	27
	d5_3	2008 Oct 01	1.27	2250	21
And VII	d7_1	2008 Aug 04	1.37	3000	65
	d7_2	2008 Aug 04	1.27	1800	38
	d7_3	2012 Sep 15	1.19	10800	64
And IX	d9_1	2009 Aug 26	1.09	2700	21
	d9_2	2009 Aug 26	1.15	2400	10
And X	d10_1	2005 Sep 05	1.41	3600	10
	d10_2	2005 Sep 05	1.2	3600	11
And XIV	A170_1	2006 Nov 20	1.24	3600	14
	A170_2	2006 Nov 21	1.2	3600	24
	d14_3	2009 Aug 22	1.02	3600	10
And XV	d15_1	2009 Aug 25	2.18	3600	18
	d15_2	2009 Aug 25	1.39	4800	10
And XVIII	d18_1	2009 Aug 26	1.3	10800	20

[a] Observations of MW GCs were not obtained as part of the SPLASH survey. More details can be found in Kirby et al. (2008, 2010, 2016).

[b] For M31 dSphs with deep ($\sim$ 6 hour total exposure time) observations, we list the observation date of the last set of observations taken.

[c] Where observations were conducted over a long timescale (e.g. months), we do not give a value for the airmass.

atmospheric parameters cover old red giant branch stars, subgiants, and lower main sequence stars: 3500 K $\leq T_{\rm eff}$ $\leq$ 8000 K, $0.0 \leq \log g \leq 5.0$, $-5.0 \leq$ [Fe/H]≤ 0.0, and $-0.8 \leq [\alpha/{\rm Fe}] \leq +1.2$ (further details of the grid can be found in Kirby et al. (2008, 2009)). Synthetic spectra are then generated using the LTE stellar synthesis code MOOG (Sneden 1973), with a resolution of 0.02Å.

3.3. *Chemical abundance pipeline*

Here we outline the pipeline we use to measure [Fe/H] and [α/Fe] for individual stars (Kirby et al. 2008; Escala et al. 2019b), which we modify to measure abundances from coadded spectra as discussed in Section 4.

3.3.1. *Telluric correction*

Spectra are corrected for absorption by the Earth's atmosphere using the method described in Kirby et al. (2008), where the observed spectrum is divided by a scaled telluric absorption template, taken from a spectrophotometric standard star (Simon & Geha 2007). For our spectra, we use BD +28 4211, observed on November 7, 2007 using the same configuration as our primary science observations.

3.3.2. *Initial continuum normalization*

The telluric-divided observed spectrum is cross-correlated with a template spectrum to determine radial velocity, as in Kirby et al. (2015), using empirical stellar templates that cover a range of effective temperature, surface gravity, and spectral types. After spectra have been corrected for telluric absorption and shifted to the rest frame, they are continuum normalized. The continuum is fit using a third-order B spline over the continuum regions (Kirby et al. 2008) with a breakpoint spacing of 100 pixels for the 1200G grating. A sigma clipping is performed (5σ tolerance, where σ is the inverse square root of the inverse variance array) to remove pixels that deviate significantly from the continuum fit. These pixels are not included in subsequent iterations of the continuum normalization. In addition to this initial normalization, we also refine the continuum fit as we solve for [Fe/H] and [α/Fe] (Section 3.3.4). In each step of the process, the continuum fit is weighted by the inverse variance of the observed spectrum.

3.3.3. *Abundance masks*

Abundance masks are constructed for measuring both [Fe/H] and [α/Fe] during the fitting procedure, to ensure that only regions sensitive to either [Fe/H] or [α/Fe] are considered. We use the same mask regions as those defined in Kirby et al. (2008). We note that the mask for [α/Fe] is constructed from regions sensitive to the individual alpha elements Mg, Ca, Si, and Ti. In addition

to these abundance masks, a general mask is applied to all spectra to exclude pixels at the beginning and end of the spectra, pixels near the detector chip gap, regions of bad sky subtraction, and other detector artifacts (Escala et al. 2019b).

3.3.4. *Measuring spectroscopic $T_{\rm eff}$, [Fe/H], [α/Fe]*

In the first stage of fitting a synthetic spectrum to the observed spectrum, effective temperature ($T_{\rm eff}$) and iron abundance ([Fe/H]) are allowed to vary simultaneously. An abundance mask is applied to consider only regions sensitive to changes in [Fe/H].

The photometric temperature is used as a starting point for the fit, with [Fe/H] initialized at -2.0 dex, and [α/Fe] initialized at 0.0 dex. We note that the choice of initial values does not affect the final measured abundances (Escala et al. 2019b). We assume the spectral resolution ($\Delta\lambda$) is a function of wavelength, determined from measuring the Gaussian widths of over 100 approximately evenly spaced sky lines for each slitmask (Kirby et al. 2008). This is a departure from the method presented in Escala et al. (2019b), where they fit for $\Delta\lambda$ due to a lack of sky lines at bluer wavelengths in the wavelength range they use in their study ($\sim 4500 - 9100$ Å). These parameters ($T_{\rm eff}$, [Fe/H]) are allowed to vary iteratively until a best fit is found.

In the next step of fitting, the best fit values of $T_{\rm eff}$ and [Fe/H] determined in the previous step are held constant, and [α/Fe] is allowed to vary. A mask is applied to consider only regions sensitive to changes to [α/Fe], in an analogous way to the mask for [Fe/H].

Using the best fit values for $T_{\rm eff}$, [Fe/H], and [α/Fe], the continuum level is then refined by dividing the continuum-normalized observed spectrum by the best fit interpolated synthetic spectrum, and fitting a third-order B-spline to this "flat-noise" spectrum with 3σ clipping. The spline fit is then subtracted from the continuum-normalized observed spectrum. The effective temperature fitting, abundance fitting, and continuum refinement process are repeated iteratively until the best fit values vary by less than 1 K, 0.001 dex, and 0.001 dex for $T_{\rm eff}$, [Fe/H], and [α/Fe], respectively. A flag is included in the final output where this continuum refinement step does not converge after 50 iterations.

The fit uncertainty is calculated from the reduced χ^2 and the covariance matrices of the fit between the best fit synthetic spectrum and the observed spectrum. For the systematic uncertainty, we adopt the same uncertainty floors as Gilbert et al. (2019): 0.101 dex for [Fe/H] and 0.084 dex for [α/Fe]. This systematic uncertainty is determined by comparing abundance measurements from high resolution spectra with those from the medium-

resolution DEIMOS spectra for a set of validation stars, and requiring that these values agree within 1σ (Kirby et al. 2009). The total uncertainty is then determined from adding in quadrature the fit and systematic uncertainties.

For our validation sample, we require that they have "good" spectra, i.e., no problems with sky subtraction or artifacts in the spectra that would be apparent upon visual inspection. Additionally, we examine the χ^2 contours of the $T_{\rm eff}$, [Fe/H], and [α/Fe] fits for each star, and remove any stars that have contours that are not smooth and continuous across the parameter range, and therefore less likely to provide reliable spectroscopic parameters. Finally, for our validation sample (Section 5), we require that stars have uncertainties of less than 0.4 dex in both [Fe/H] and [α/Fe], their spectra converged during the continuum refinement step in the synthetic spectral pipeline, and their measured abundances do not hit the limits of the synthetic spectral grid.

4. COADDING SPECTRA

After we measure spectroscopic $T_{\rm eff}$, [Fe/H], and [α/Fe] for all stars in our MW GC and M31 dSph samples using the pipeline described above, we apply a number of membership cuts to ensure that we only select stars that are highly likely to belong to the object in question. In addition, we apply a set of quality criteria to select a set of stars that will be used for validating our pipeline (Section 5.2). We refer to the coadds using these stars as "validation coadds". Any stars which pass the membership criteria but do not pass the quality criteria we consider our science sample, and we refer to coadds constructed from this sample of stars as our "science coadds".

4.1. *Membership and quality criteria*

To ensure membership for stars in our globular cluster sample ($\langle S/N\rangle = 158.13$ per angstrom), we use the $(I, V - I)$ CMD to select only those stars that fall on the RGB or AGB. We also require that stars satisfy $\log g < 3.6$ to ensure that they are giants.

For our sample of stars in M31 dSphs, we adopt the criteria used previously for analysis of these samples. We describe below the differences between the membership selection used for masks with deep observations, and those with shallow observations. For our M31 dSphs with deep (~ 6 hr, $\langle S/N\rangle = 15.3$ per angstrom) observations, we identify dSph members using a two-step process. First, we use the M31/MW membership classification scheme described by Gilbert et al. (2006) to identify stars that are likely to be RGB stars at approximately M31's distance, rather than foreground MW dwarf stars.

This membership classification is based on a number of criteria including radial velocity, a star's position in $(M - {\rm DDO51})$ versus $(M - T_2)$ color-color space, its position in $(I, V - I)$ color-magnitude space, and the equivalent width of the Na I doublet at 8190 Å ($\lambda\lambda$ 8183,8195). We note that the membership classification for our dSphs assumes M31's distance modulus. Therefore, we consider stars to be a dSph member if they are more probable to be an M31 RGB star than a MW foreground star based on the above diagnostics. We make an exception for stars that are slightly too blue for the most metal-poor isochrone at the distance of M31, and would otherwise be classified as MW foreground stars. We include these stars in our membership selection because they are likely to belong to the M31 satellite if they pass additional velocity cuts (Gilbert et al. 2006). Second, we require that all stars that satisfy the M31 RGB criteria also explicitly fall within the expected radial velocity limits for a given M31 dSph, listed in Table 2. These velocity limits correspond to approximately the difference between the mean systemic velocity and three times the velocity dispersion for a given dSph (see Table 3 of Kirby et al. 2020).

For M31 dSph stars with shallow ($\sim$ 1-2 hour, $\langle S/N\rangle = 7.6$) observations, we adopt the M31 dSph membership criteria described by Tollerud et al. (2012). This membership determination simultaneously evaluates the probability the star is an RGB star at the distance of the M31 system, as well as a member of the dSph. It relies on three probabilistic criteria: the distance between a given star and the dSph to which it lies near, a star's position in $(T_2, M - T_2)$ color-magnitude space, and the equivalent width of the Na I doublet. In addition, a "wide selection window around the dSphs systemic velocity" (Tollerud et al. 2012) is used to remove obvious outliers from their dSph membership. These four criteria are then used to calculate the probability of a star being a member of a given dSph (see Eq. 1 of Tollerud et al. 2012), where stars having a membership probability greater than 0.1 are selected as dSph members. We include the systematic velocities of these dSphs with shallow observations in Table 2 for completeness.

4.2. *Selecting groups for coaddition*

We adopt two binning strategies: sorting stars by either photometric $T_{\rm eff}$ or photometric metallicity ([Fe/H]$_{\rm phot}$), and then binning them such that each coadd has at least five stars. We find, as in Yang et al. (2013), that the final measured abundances are consistent when stars are grouped by either photometric temperature or metallicity, so for the purposes of our analysis we simply use the photometric metallicity. The
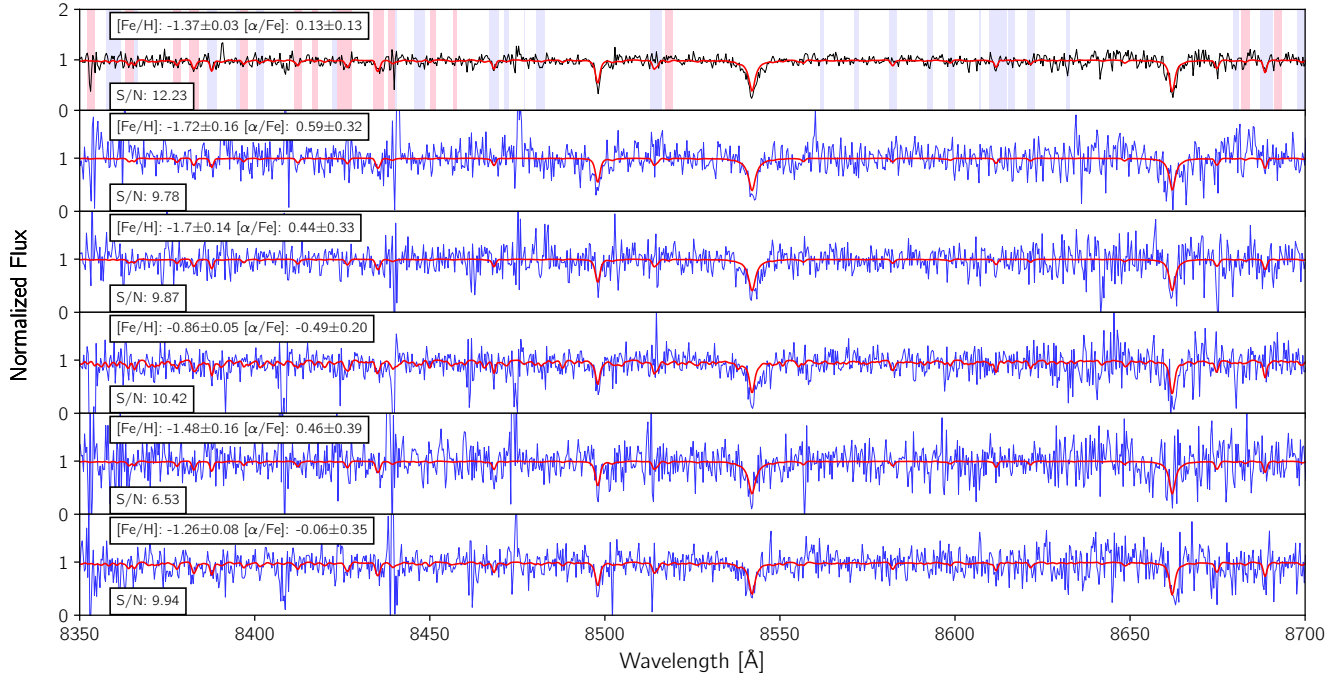
Figure 1. A coadded spectrum (top panel) using spectra from d7_1, a dSph mask with shallow spectroscopic observations. Signal-to-noise, derived spectroscopic [Fe/H] and [α/Fe] are given in each panel, with the best fit synthetic spectrum overplotted in red. Regions sensitive to a given abundance and included in the fitting process are indicated in light blue and pink for [Fe/H] and [α/Fe], respectively. Spectra of the five RGB stars used in constructing the coadded spectrum are shown in the bottom five panels in blue. The coadded spectrum illustrates the improvement in S/N (and therefore our ability to measure abundances) over the individual spectra.

Table 2. Kinematic properties of M31 dSphs.

Object name	$\langle v_{\mathrm{helio}} \rangle$	σ_v	Velocity Limits	Reference[a]
	(km s^{-1})	(km s^{-1})	(km s^{-1})	
And I	$-378.0^{+2.4}_{-2.3}$	$9.4^{+1.7}_{-1.5}$	$[-390, -340]$	1
And II	-192.4 ± 0.5			2
And III	$-348.0\pm^{+2.7}_{-2.6}$	$11.0^{+1.9}_{-1.6}$	$[-370, -320]$	1
And V	-397.7 ± 1.5	$11.2^{+1.1}_{-1.0}$	$[-440, -360]$	1
And VII	-311.2 ± 1.7	$13.2^{+1.2}_{-1.1}$	$[-340, -260]$	1
And IX	-209.4 ± 2.5			3
And X	-166.9 ± 1.6	$5.5^{+1.4}_{-1.2}$	$[-180, -140]$	1
And XIV	-480.6 ± 1.2			3
And XV	-323.0 ± 1.4			3
And XVIII	-332.1 ± 2.7			3

[a]References. 1: Kirby et al. (2020) (deep observations), 2: Ho et al. (2012) (shallow observations), 3: Tollerud et al. (2012) (shallow observations)

choice to bin by photometric [Fe/H] is motivated by the reasoning given in Yang et al. (2013), where they state that the synthetic spectra can account for a range of T_{eff} within a bin, but not [Fe/H] or [α/Fe]. For completeness, we include a brief summary of the following

analysis done with stars sorted by photometric T_{eff} in Appendix B.

A group of spectra to be coadded are then processed using the same method described above (Section 3), where they are corrected for telluric absorption and shifted to the rest frame, and an initial continuum normalization is performed. Each spectrum in the group is then rebinned to the same spectral range $(6300 - 9000\ \text{Å})$, with a wavelength spacing of 0.32 Å for the 1200 l mm^{-1} grating, to ensure that all spectra are on the same pixel array. This rebinning is applied to both the flux and inverse variance arrays for each spectrum. We then perform a two-step sigma clipping for each pixel in the group of spectra to be added. If a pixel for any spectrum in the group deviates more than 10σ or 3σ (where σ is the standard deviation of the flux for a given pixel) from the median flux for the first and second step of the sigma clipping, respectively, the pixel is masked when adding that spectrum to the coadded spectrum.

4.3. *Coaddition*

Fluxes are coadded together weighted by their inverse variance ($1/\sigma^2$):

$$\bar{x}_{\mathrm{pixel},i} = \frac{\sum_{j=1}^{n}(x_{\mathrm{pixel},ij}/\sigma^2{}_{\mathrm{pixel},ij})}{\sum_{j=1}^{n} 1/\sigma^2{}_{\mathrm{pixel},ij}} \tag{1}$$
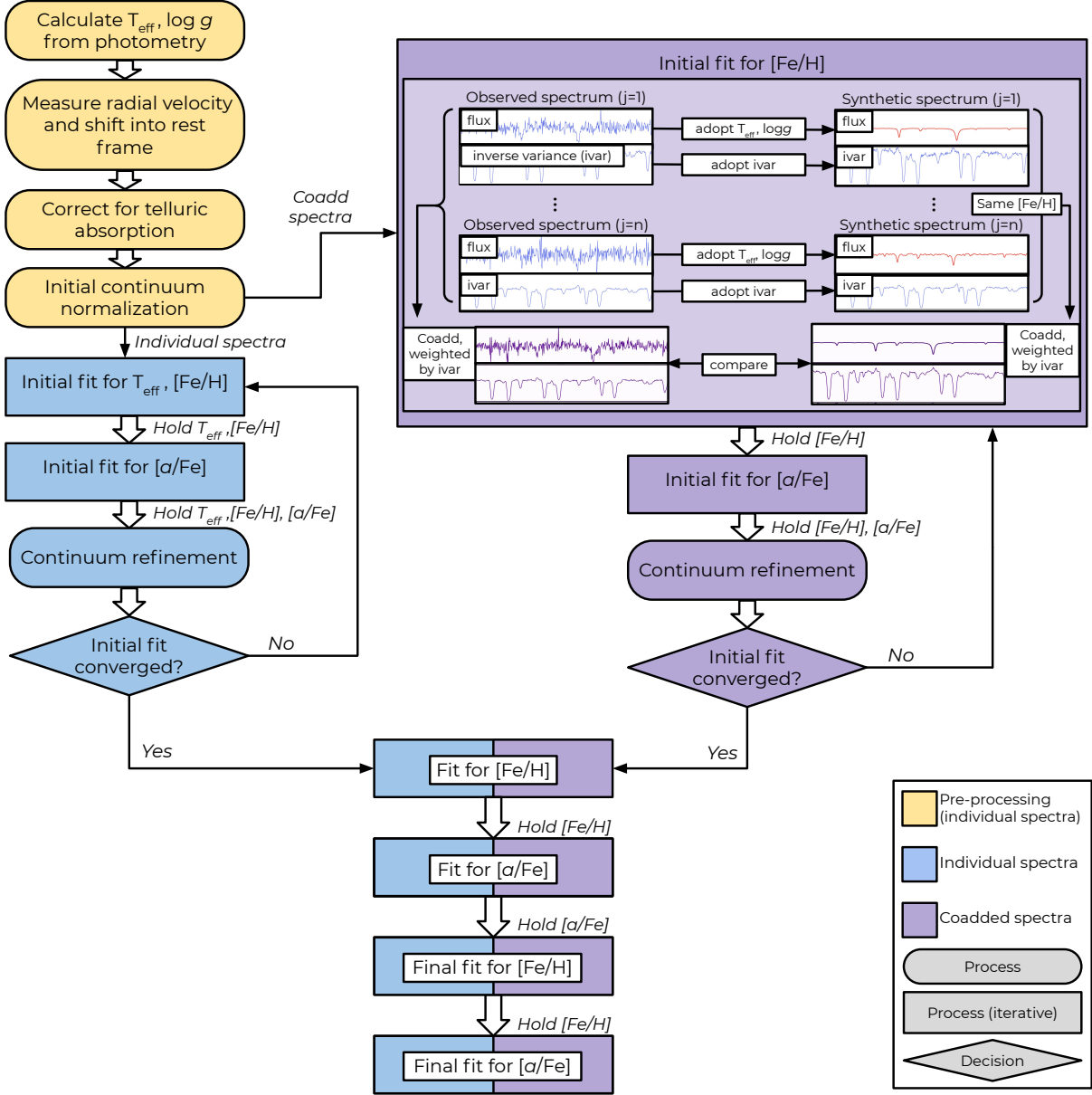
Figure 2. A step-by-step illustration of our process to determine [Fe/H] and [α/Fe] from individual (blue) and coadded (purple) spectra. Pre-processing steps are shown in yellow. Rounded rectangles indicate single-step processes, while rectangles indicate processes that involve iterating through a loop (i.e., fitting procedures). Steps indicated with a diamond represent an *if* statement. The inset on the top right shows how synthetic spectra are constructed by adopting the photometric effective temperature, surface gravity, and inverse variance array of the corresponding observed spectra.

where $x_{\mathrm{pixel},ij}$ represents the flux of the ith pixel of the jth spectrum in a group, $\sigma^2_{\mathrm{pixel},ij}$ is the corresponding variance of $x_{\mathrm{pixel},ij}$, and n is the total number of spectra to be coadded. The inverse variance weighted flux of the ith pixel of the coadded spectra is then given by $\bar{x}_{\mathrm{pixel},i}$. The inverse variance of the coadded spectra is:

$$\bar{\sigma}_{\mathrm{pixel},i} = \left(\sum_{j=1}^{n} \frac{1}{\sigma^2_{\mathrm{pixel},ij}} \right)^{-1/2} \qquad (2)$$

Figure 1 shows a small portion of the full spectral range for an example coadd, where the final coadded spectrum and the corresponding best-fit synthetic spectrum (red) are shown in the top panel, and the individual constituent spectra are shown in the lower panels.

4.4. *Measuring abundances from coadded spectra*

To ensure an accurate comparison between our observed coadded spectra and the synthetic spectral grid, we coadd synthetic spectra using the same procedure

as the observed spectra (Eq. 1). During each abundance determination step, from the synthetic spectral grid, we select a group of synthetic spectra with temperatures and surface gravities that correspond to the $T_{\rm eff}$ and $\log g$ (determined from photometry) for each observed spectrum. The synthetic spectra are rebinned to the same wavelength range and pixel scale as the observed spectra, and are smoothed with a Gaussian filter to replicate the spectral resolution of the observed spectra, where the method to determine the spectral resolution is described in Section 3.3.4. The synthetic spectra are then weighted by the same inverse variance array (Eq. 2) as their corresponding observed counterparts to produce a coadded synthetic spectrum for each iteration of the fitting procedure.

The process for measuring abundances from coadded spectra varies slightly from the process outlined in Section 3. When finding the best fit between our coadded observational spectrum and coadded synthetic spectra, we use photometric $T_{\rm eff}$ and $\log g$ estimates from each observed star for their counterpart in the coadded synthetic spectrum in each iteration of the fit. We first fit only [Fe/H], keeping [α/Fe] fixed, and then fit [α/Fe], keeping [Fe/H] fixed, using the same masks described in Section 3.3.3 for these abundance measurements. We refine the continuum of the coadded spectrum as described in Section 3.3.4. We iterate over these three steps (fitting [Fe/H], [α/Fe], and continuum refinement) until the measured values for [Fe/H] [α/Fe] change by less than 0.001 dex on consecutive passes.

We then take the coadded spectrum with its refined continuum and fit for [Fe/H], taking the [α/Fe] value from the last iteration of the continuum refinement. We repeat this process for [α/Fe], keeping [Fe/H] constant from the previous step, and adopt this value as our final measured [α/Fe]. Finally, we refit for [Fe/H] using the final measured [α/Fe], and take the value of [Fe/H] from this step as our final measured [Fe/H]. After this round of fitting [Fe/H] and [α/Fe], we check the goodness of the fit. For our coadded abundance measurements, we apply the same quality criteria as in Section 3. In addition, we examine the χ^2 contours for [Fe/H] and [α/Fe] to ensure the minimum is well-defined.

5. PIPELINE VALIDATION AND ESTIMATING UNCERTAINTIES FOR COADDED SPECTRA

Validation was done using the six MW globular clusters (NGC 2419, NGC 6656, NGC 1904, NGC 6341, NGC 6864, NGC 7078), four M31 dSphs that have both deep observations and shallow observations (And I, And III, And V, And VII), one dSph that has validation stars from deep observations only (And X), and one

M31 satellite with shallow observations only (And II). The number of individual stars and validation coadds for each slitmask for each of these three samples can be found in Table 3. Here, we define our "validation coadds" as coadds composed of stars that individually have both [Fe/H] and [α/Fe] uncertainties less than 0.4 dex, and have a χ^2 minimum that is not at the edge of the synthetic spectral grid (-5.0 or 0.0 for [Fe/H], -0.8 or 1.2 for [α/Fe]). In total, our validation sample consists of 37 validation coadds from GC masks, 24 from M31 dSph masks with deep observations, and 9 from M31 dSph masks with shallow observations. Figure 3 shows the distribution in S/N for each of our three samples, illustrating the S/N regime probed by each. The MW GC sample contains the highest quality spectra with respect to S/N, and provides a first check for the efficacy of our pipeline. The M31 dSph samples allow us to test the coaddition pipeline at lower S/N regimes, where different sources of noise may hinder our ability to determine chemical abundances. In particular, the M31 dSph sample from shallow observations provides a probe of the lowest S/N at which we can reliably measure chemical abundances from individual spectra (S/N $\gtrsim 8$ per Angstrom, although we do not apply a strict S/N cut for individual spectra to any of our samples).

5.1. Uncertainties on coadded spectra

For our coadded spectra, we consider two sources of uncertainties on [Fe/H] and [α/Fe]. First, we estimate the fit (or statistical) uncertainty from the diagonals of the covariance matrix and the reduced chi-square value (χ^2) of the fit. For either [Fe/H] or [α/Fe], we take into account the same spectral mask (Section 3.3.3) used in the fit, in order to only consider regions of the spectrum sensitive to either [Fe/H] or [α/Fe]. We also consider the effect of uncertainties on the photometric $T_{\rm eff}$ and $\log g$ values as part of the fit uncertainty. The process used to estimate this portion of the fit uncertainty is described in Section 5.1.1. Second, we consider the systematic uncertainties, which encompass all other sources of unknown uncertainty in our fits (Section 5.1.2).

5.1.1. Estimating fit uncertainties due to uncertainties from photometric stellar parameters

In measuring [Fe/H] and [α/Fe] for each star we adopt values for $T_{\rm eff}$ and $\log g$ derived from photometry. These values are propagated through our pipeline to the comparison with synthetic spectra (Section 4.4). As we do not fit for $T_{\rm eff}$ or $\log g$, we estimate the component of the fit uncertainty due to uncertainties in these photometric stellar parameters. We assume the photometric $T_{\rm eff}$ and $\log g$ uncertainties are Gaussian, and draw 50
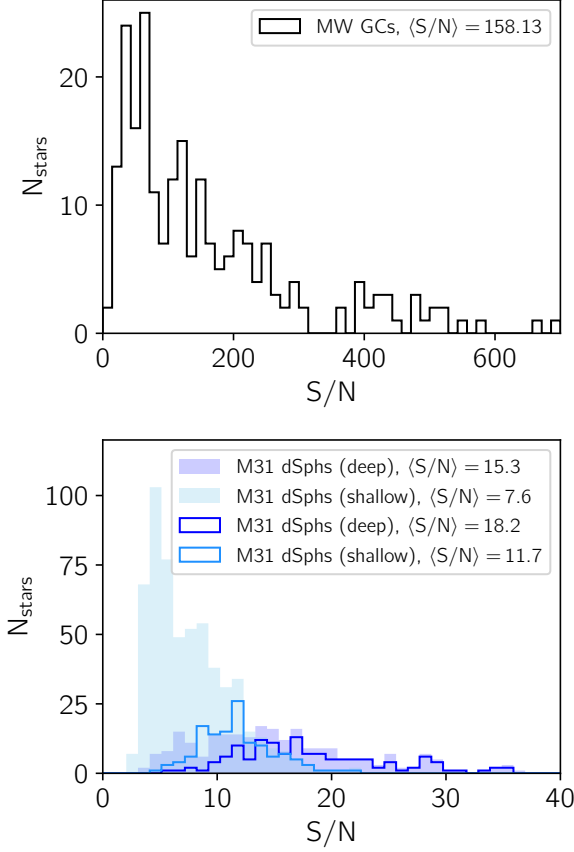
Figure 3. Histograms showing the distribution of S/N (per angstrom) of individual stars in our Milky Way globular cluster sample (top) and our validation M31 dSph stars (bottom). The solid-filled histograms represent the entire sample of member stars, with the lines showing the sample used for validating our coaddition pipeline (Section 5.2).

Table 3. Validation Sample

Object name	Slitmask	N_{stars}	N_{coadds}
MW GCs			
NGC 2419	n2419c	49	9
NGC 6656 (M22)	n6656b	35	7
NGC 1904 (M79)	1904l1	18	3
NGC 6341	n6341	25	5
NGC 6864	n6864	36	7
NGC 7078 (M15)	7078l2	33	6
M31 dSphs			
Deep observations			
AndI	and1a	16	3
AndIII	and3a	17	3
AndV	and5a	28	4
	and5b	23	4
AndVII	and7a	58	9
AndX	and10b	3	1
Shallow observations			
AndI	d1_1	7	1
	d1_2	11	1
AndII	d2_1	15	2
AndIII	d3_1	7	1
AndV	d5_1	9	1
AndVII	d7_1	16	3

random samples from the covariant T_{eff}–$\log g$ distributions for each star in a given coadd. We then remeasure [Fe/H] and [α/Fe] for each of these samples for each coadd. We then take the standard deviation of the abundance measurements from all samples for a given coadd as the typical uncertainty due to the photometric T_{eff} and $\log g$ (σ_{MC}), and add this uncertainty in quadrature to the fit uncertainty (σ_{fit}) to get our total fit uncertainty for both [Fe/H] and [α/Fe]:

$$\sigma_{fit,total} = \sqrt{\sigma_{fit}^2 + \sigma_{MC}^2} \quad (3)$$

The magnitude of this uncertainty is small compared to the fit uncertainty, with median values of approximately 0.02 dex for [Fe/H] and 0.01 dex for [α/Fe].

5.1.2. *Quantifying systematic uncertainties*

We estimate the systematic uncertainties on our coadded abundance measurements by estimating the uncertainty term needed to enforce that the measurement

from the coadd agrees with the weighted average within one standard deviation. We compute this using all validation coadds from all GCs:

$$\frac{1}{\sum_i N_i - 1} \sum_{i=1}^{N_{GC}} \sum_{j=1}^{N_i} \frac{(X_{coadd,i,j} - \langle X_i \rangle)^2}{\sigma_{fit,coadd,i,j}^2(X) + \sigma_{sys}^2(X)} = 1 \quad (4)$$

where i indicates a given GC, j indicates a given coadd for that GC, N_{GC} is the number of GCs in our sample (6), and N_i is the number of coadds in the ith GC. The coadded abundance value in a given GC for X = [Fe/H] or [α/Fe] is $X_{coadd,i,j}$, $\sigma_{coadd,i,j}(X)^2$ is the fit uncertainty for that measurement, and $\langle X_i \rangle$ is the weighted average abundance from the coadds for a given GC. We then numerically solve for $\sigma_{sys}^2(X)$, for both [Fe/H] and [α/Fe]. With our sample of GCs, we measure a systematic uncertainty of 0.02 dex for [Fe/H] and 0.07 for [α/Fe]. Figure 4 shows the uncertainty-weighted [Fe/H] and [α/Fe] distributions for the validation coadds in each GC (colored histograms), and for all GCs (black histogram). A Gaussian with the standard deviation equal to the derived systematic uncertainty is overplotted. The width of this Gaussian corresponds to how well the expected

uncertainties capture the total uncertainties in our sample. A best-fit Gaussian that is narrower than a unit Gaussian would indicate that we overestimate our uncertainties, while a best-fit Gaussian that is wider than a unit Gaussian would indicate that we underestimate our uncertainties.

We find the systematic uncertainty for our GC sample to be of the order of their fit uncertainties. Therefore, we adopt the same systematic uncertainty floors as in Gilbert et al. (2019) for spectra measured with the 1200G grating: 0.101 dex for [Fe/H], and 0.084 dex for [α/Fe]. The total uncertainty on our coadded abundance measurements ($\sigma_{\rm total,coadd}(X)$) is then:

$$\sigma_{\rm total,coadd}(X) = \sqrt{\sigma^2_{\rm fit,coadd} + \sigma^2_{\rm sys}} \qquad (5)$$

where $\sigma^2_{\rm fit,coadd}$ is the fit uncertainty as described in Section 5.1.1, and $\sigma^2_{\rm sys}$ is the systematic uncertainty corresponding to the systematic uncertainty floor for either [Fe/H] or [α/Fe] as given above.

5.2. Comparison between coadded and weighted average abundances

To test the accuracy of our pipeline, we compare the inverse variance weighted average [Fe/H] and [α/Fe] from measurements of individual spectra with that measured from coadded spectra. We would expect similar results if a coadded spectrum is truly representative of the weighted average of its constituents.

To compute the average inverse variance weighted abundance of a group of spectra, we define the following weights (ω_j), following Yang et al. (2013):

$$\sigma^2_{\rm spec,j} = \left(\sum_{i=1}^{\rm mpixel} (\sigma_{{\rm pixel},ij})^{-2} \cdot M_{{\rm element},X} \right)^{-1} \qquad (6)$$

$$\omega_j(X) = \frac{1/\sigma^2_{\rm spec,j}}{\sum_{j=1}^n 1/\sigma^2_{\rm spec,j}} \qquad (7)$$

where mpixel is the total number of pixels in a spectrum, $\sigma_{{\rm pixel},ij}$ is the variance of the ith pixel of the jth spectrum in a group, and $M_{{\rm element},X}$ is the corresponding elemental mask for fitting X, where X is either [Fe/H] or [α/Fe]. The weighted variance for the jth spectrum is $\sigma^2_{\rm spec,j}$, and $\omega_j(X)$ is the weight of either [Fe/H] or [α/Fe] for the jth star of n stars in a coadded group. The weighted average abundance is then:

$$X_{\rm bin,wa} = \sum_{j=1}^n \omega_j(X) X_j = \frac{\sum_{j=1}^n X_j/\sigma^2_{\rm spec,j}}{\sum_{j=1}^n 1/\sigma^2_{\rm spec,j}}. \qquad (8)$$

The weighted uncertainty on the weighted average abundance is given as:
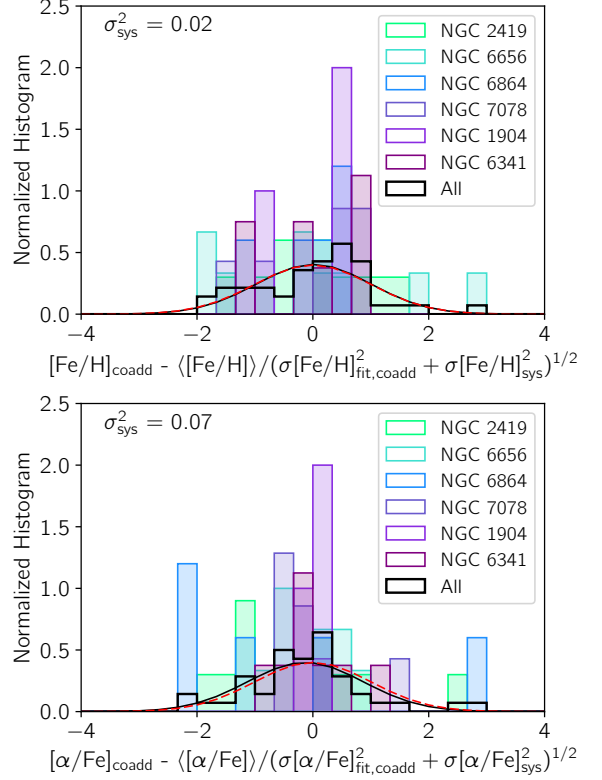
Figure 4. Histogram of the differences between coadded abundances and weighted averages, weighted by their corresponding uncertainties, for [Fe/H] (top) and [α/Fe] (bottom). The solid black histogram represents the normalized sum of all validation coadds for all GCs in our sample. The solid black curve indicates the best-fit Gaussian for the sample of all validation coadds from all GCs, and the dashed red curve indicates a normalized unit Gaussian with $\sigma = 1$.

$$\sigma^2_{\rm bin,wa}(X) = \omega^2_j(X) \sigma^2_{\rm total,j}(X), \qquad (9)$$

$$\sigma_{\rm total,j}(X) = \sqrt{(\sigma_{\rm fit,j}(X))^2 + (\sigma_{\rm (sys}(X))^2} \qquad (10)$$

where we adopt the systematic uncertainties of 0.101 dex for [Fe/H], and 0.084 dex for [α/Fe], from Kirby et al. (2020), where the method used to measure these values is described by Kirby et al. (2010).

In Figures 5, 6, and 7, we compare the weighted average [Fe/H] and [α/Fe] from measurements of individual spectra with their measurements from coadds for MW GCs, M31 dSphs with deep observations, and M31 dSphs with shallow observations, respectively. In each consecutive plot, we include the points from the previous plot (as grey points), for reference and to illustrate the range in [Fe/H] and [α/Fe] that each sample covers.
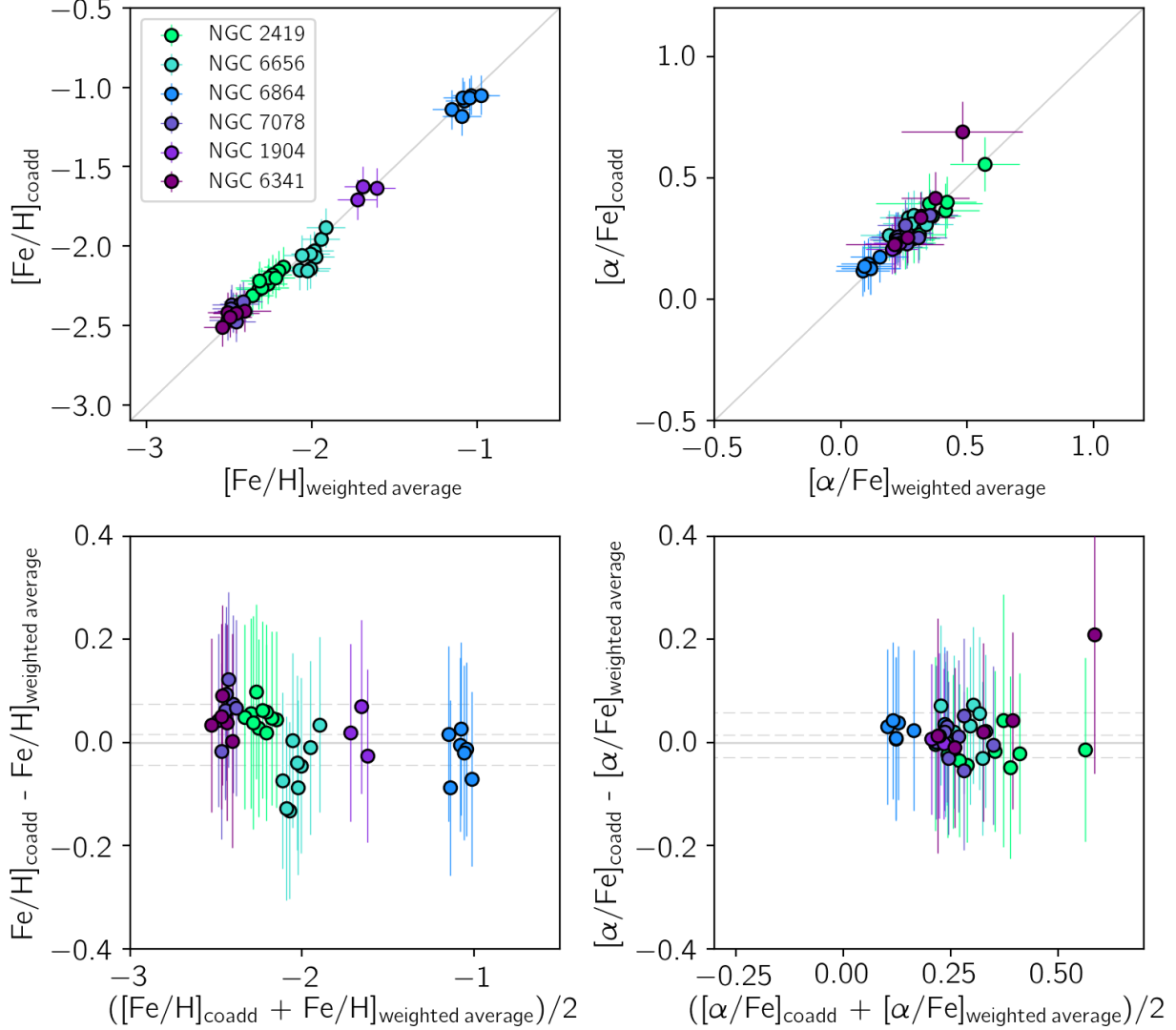
5.2.1. Milky Way globular clusters

Figure 5. Top: Comparison between the weighted-average abundances with those measured from coadded spectra, for six Milky Way globular clusters. Bottom left: residuals of the difference between the weighted-average abundances and those measured from coadded spectra. The dashed grey lines indicate the mean and standard deviation of the difference. The weighted average [Fe/H] and [α/Fe] values are determined as described in Section 5.2. Values for the mean and dispersion of the residuals are given in the text. As the offset and dispersion are smaller than the average total uncertainty, we conclude that the measurement from our coaddition method accurately recovers the weighted average of abundance measurements from individual stars in a given coadd.

Our MW GC sample includes stars that are much closer (average distance 23 kpc), and are therefore much brighter (average $\sim$ 4 mag brighter in V-band) than RGB stars in M31 dSphs. For these GC stars, we obtain high S/N spectra, which in turn provide a higher degree of certainty on their individual chemical abundance measurements. Because GCs are principally single stellar populations, we also can safely assume that the metallicity ([Fe/H]) distribution function of these GCs is roughly single-valued, and can therefore more clearly identify outliers in [Fe/H]. In Figure 5, we show

the comparison between the weighted average [Fe/H] and [α/Fe] from individual stars to those measured from the coadds. From the residuals (bottom row of Figure 5), we find an average offset of -0.008 dex in [Fe/H] with a dispersion of 0.057 dex. We consider this to be very good agreement between the weighted-average and coadded abundance measurements, across the large range of [Fe/H] that our GCs probe. In general, we do not find any trend in the difference as a function of metallicity. For [α/Fe], we find an average difference of 0.027 dex, with a dispersion of 0.033 dex. Again, we
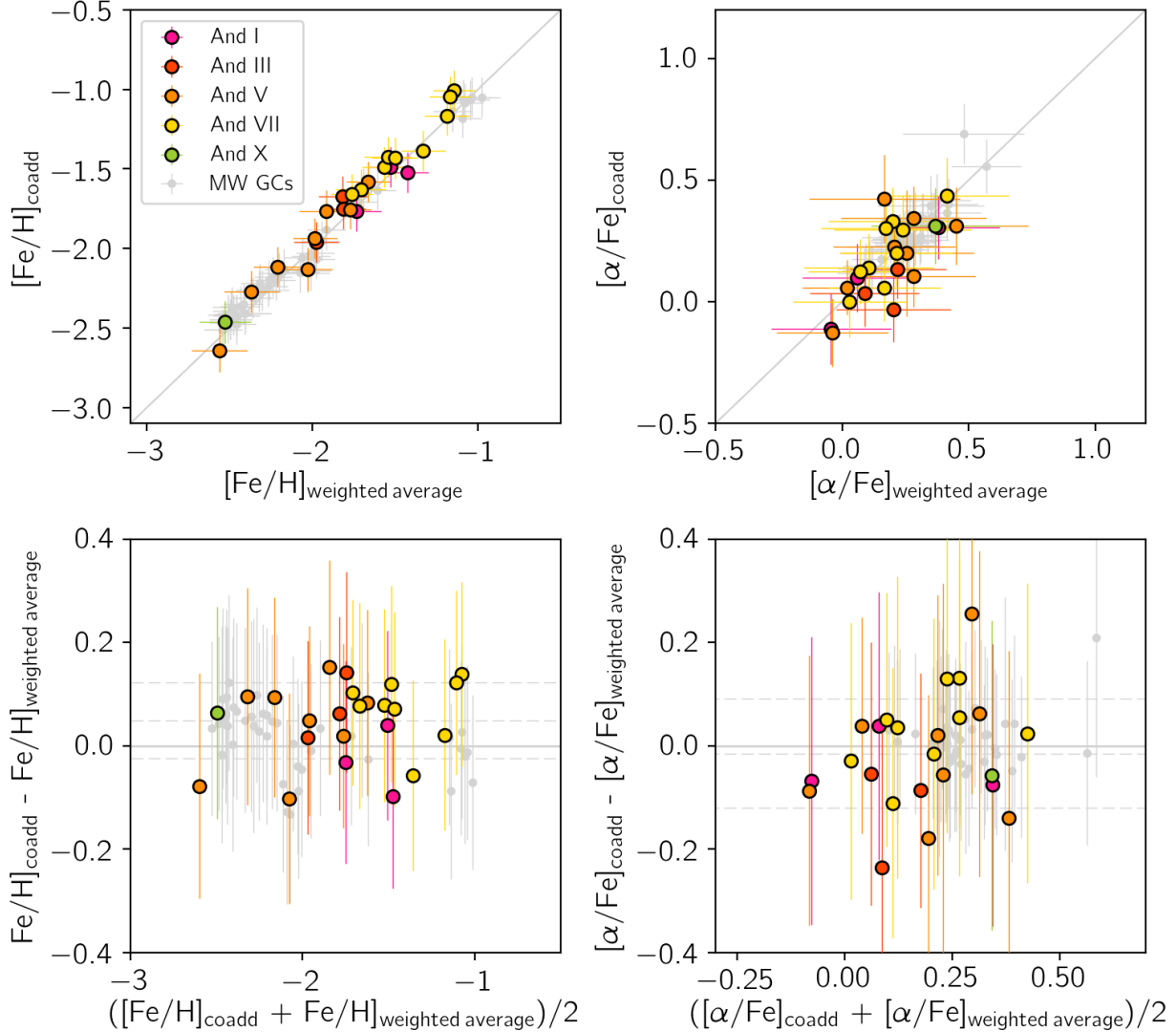
Figure 6. The same as Figure 5, with the colored points indicating our sample of validation coadds from M31 dSphs with deep observations ($\langle S/N = 18.2 \rangle$), and the grey points indicating the same MW GCs from Figure 5.

consider this to be very good agreement between the weighted average and coadded $[\alpha/\text{Fe}]$ measurements, as we find no significant offset in the difference, and the dispersion is less than the adopted systematic uncertainty.

5.2.2. *M31 dSphs with deep observations*

Figure 6 shows the same comparison as Figure 5, but now with the colored points showing our groupings for M31 dSph stars with deep observations ($\langle S/N = 18.2 \rangle$, see Figure 3). In this figure we also include MW GC groupings, for comparison, in grey. For [Fe/H], we measure an average difference of 0.042 dex, with a dispersion of 0.076 dex, and for $[\alpha/\text{Fe}]$, we measure an average offset of -0.007 dex with a dispersion of 0.099 dex. While the spread in differences is larger for this sample, any offset and associated dispersion is small compared to the

total uncertainty for the coadded measurements. For both [Fe/H] and $[\alpha/\text{Fe}]$, we do not find any trend in the difference as a function of [Fe/H] or $[\alpha/\text{Fe}]$.

5.2.3. *M31 dSphs with shallow observations*

In Figure 7 we consider our sample of M31 dSphs for which we have shallow observations (colored points), with MW GCs and deep dSph samples for comparison in light grey and grey, respectively. This sample contains, on average, stars with much lower S/N spectra ($\langle S/N = 11.7 \rangle$, see Figure 3). For [Fe/H], we find an offset of 0.022 dex with a dispersion of 0.066 dex, and for $[\alpha/\text{Fe}]$, we find an offset of -0.053 dex, with a dispersion of 0.074 dex, and no trend in difference with measured abundance for either [Fe/H] or $[\alpha/\text{Fe}]$. We find, in general, that the difference between the weighted-average
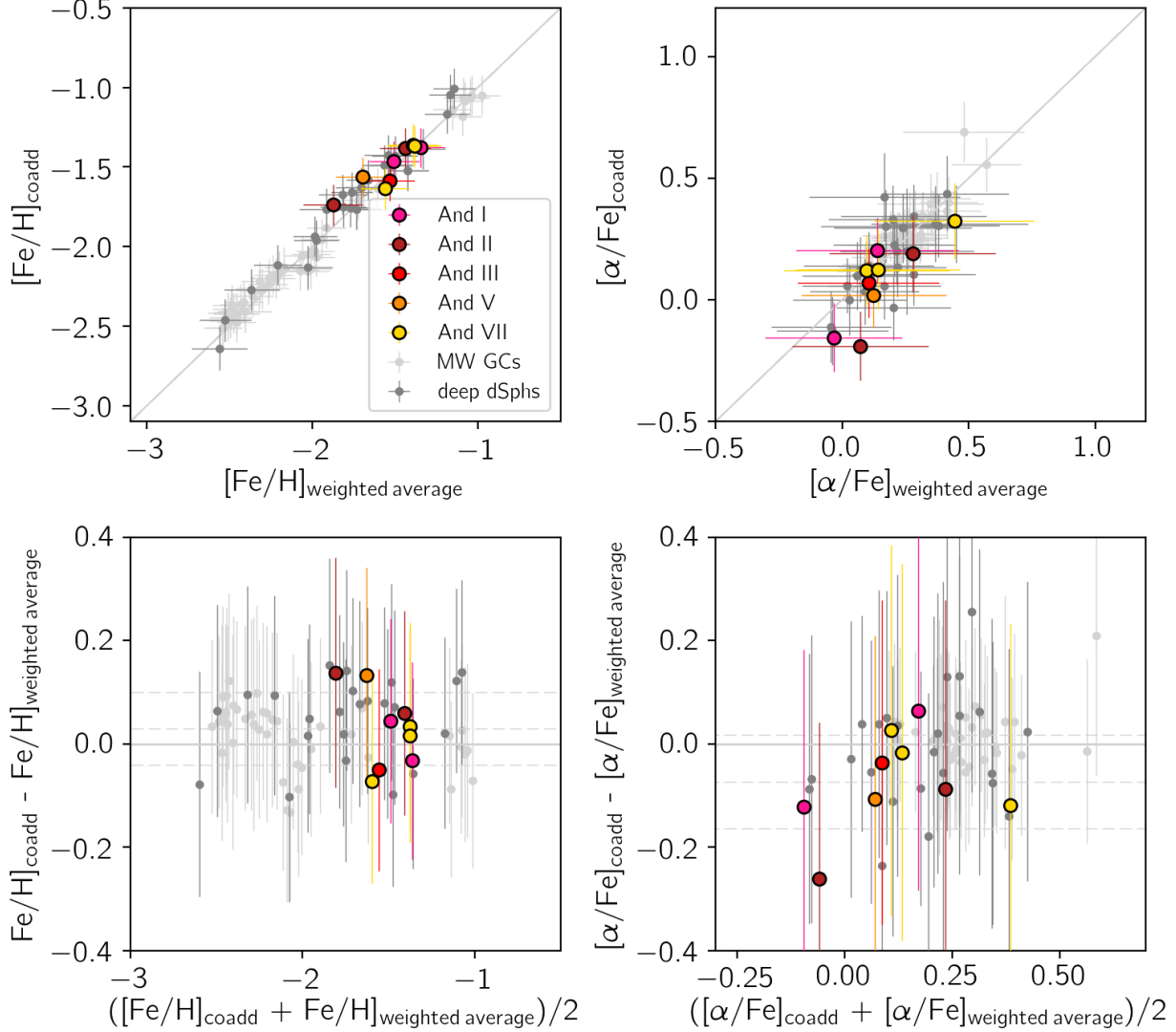
Figure 7. The same as Figure 6, with the colored points indicating our sample of M31 dSphs with shallow observations ($\langle S/N = 11.7 \rangle$), and the light and dark grey points indicating the same Milky Way globular clusters and M31 dSphs with deep observations from Figures 5 and 6, respectively.

and coadded abundances for shallow M31 dSph spectra is consistent with those from deep observations, illustrating the performance of our method at the lower end of the S/N regime.

If we consider all three samples simultaneously, we find an average offset in [Fe/H] of 0.015 dex, with a dispersion of 0.074 dex, and for [α/Fe], we find an offset of 0.002 with a dispersion of 0.076 dex. Unlike Yang et al. (2013), we do not find any trend in average difference as a function of [Fe/H] or [α/Fe] for any of our samples (see their Figure 8). These offsets are approximately an order of magnitude lower than the systematic uncertainty floors (0.101 for [Fe/H], 0.084 for [α/Fe]). As a result, we conclude that our coaddition method accurately re-

produces the same [Fe/H] or [α/Fe] measurement as the weighted average of the individual spectra in a group.

6. COADDING SPECTRA WITH LARGE UNCERTAINTIES ON THEIR INDIVIDUAL ABUNDANCE MEASUREMENTS

So far, we have only considered stars for which we have secure abundance measurements, i.e., uncertainties in [Fe/H] and [α/Fe] less than 0.4 dex, and the χ^2 minimum is not at the edge of the grid of synthetic spectra ([$-5, 0.0$] for [Fe/H], [$-0.8, 1.2$] for [α/Fe]). However, our aim is to test the application of our method to stars in M31 where we cannot reliably measure abundances individually (most of the spectra in SPLASH). Therefore, for the following analysis, we consider only stars

from the M31 dSph slitmasks. In addition, for the purposes of investigating the abundance distributions, we no longer consider deep and shallow coadds separately, combining both sets of coadds to obtain the abundance distribution for a given slitmask. We will refer to the coadds used for validation as our "validation coadds", and the coadds that were not used for validation as "science coadds". Our coadded abundance measurements for both [Fe/H] and [α/Fe] for both validation and science coadds can be found in Table 4.

We apply the same M31 dSph membership criteria as described in Section 4.1, now coadding only those spectra where the individual abundance measurements did not satisfy the quality criteria. We now also consider additional slitmasks for which we only have shallow (∼ 1 − 2 hr) observations, adding And IX, XIV, XV, and XVIII to our sample of M31 dSphs. This increases our sample size to ten total satellite galaxies. We then apply the same coaddition method as described in Section 4. Table 5 gives a summary of the science coadds for each slitmask.

For these science coadds, we cannot directly compare abundance measurements from the coadded spectra with those from the weighted average, as they do not have reliable individual [Fe/H] and/or [α/Fe]. Instead, we compare the distribution of these measurements with that of the validation sample, i.e., where latter consists of the individual stars having reliable measurements.

In Figure 8, we show histograms of spectroscopic [Fe/H] measurements for three samples: individual measurements (solid grey), validation coadds (solid colored lines), and science coadds (dashed colored lines). The ten M31 dSphs in our sample are sorted roughly by their stellar mass. We note that And V is out of order with respect to mass, but we keep it in the left-hand column as the sample size is more akin to those in the left-hand column.

We use a set of statistical tests to determine how the [Fe/H] distribution of our science coadds compares to the underlying distribution of individual stars that they should represent. First, we calculate the Kolmogorov-Smirnov statistic between the distribution of individual stars and both the validation coadds, and between the individual stars and science coadds. For dSphs that have stars with both individual abundance measurements and validation coadds, we find that the K-S test cannot reject the null hypothesis that the two distributions are the same. Some caution is warranted for the dSphs for which we have only a few individual or coadded measurements (And XVIII, XV, XIV, IX, X), as this test may be less reliable, due to the sparse sampling of the abundance distributions.

When we compare abundance measurements from individual stars to our science coadds, we find that, for three dSphs in our sample (And VII, III, and V), the null hypothesis can be rejected, i.e., it is more likely that the samples are not drawn from the same distribution. For these three dSphs, we also perform Welch's t-test between the distribution of validation and science coadds, to test if the two distributions have similar means, though not necessarily similar population variances. With this test, we find that the distributions of the validation and science coadds agree for And III and V, but the null hypothesis is rejected for And VII. We find that while the distribution of science coadds fits within the distribution of individual abundance measurements for the majority of our M31 dSphs, there is a slight shift in the distribution mean between the validation coadds and the science coadds. The distributions of science coadds tend to be more metal-poor than the validation coadds. We note that this is somewhat expected, as it is more difficult to determine abundances for an individual metal-poor star compared to a metal-rich star in this low S/N regime, owing to the depth of the spectral features. Therefore, these stars may be less likely to be part of the validation sample, and more likely to be used for the science coadds.

In general, we find that our science coadds agree with the distribution from our validation sample, and fit within the distribution of individual abundance measurements. We further expand on this comparison by exploring the 2D [Fe/H]–[α/Fe] chemical space in the following section.

7. DISCUSSION AND APPLICATIONS
7.1. *The [α/Fe]–[Fe/H] plane*

In Figure 9, we present the [α/Fe]–[Fe/H] distributions for the ten M31 dSphs in our sample, with measurements from individual stars indicated by transparent grey circles, measurements from validation coadds with solid circles, and measurements from science coadds with diamonds. Measurements made from shallow data are color-coded according to a galaxy's stellar mass, and measurements made from deep data are shown in grey. The dSphs are sorted approximately by mass, so that the relationship of decreasing average metallicity with decreasing mass is easily visible. As in Figure 8, we keep And V in the left-hand column, as it more relevant to compare it to the more massive satellites with a larger sample size. The less-massive dSphs are more sparsely sampled, but we find they still follow roughly the same trend (see Section 7.3 for an in-depth discussion). We note that for four dSphs in our sample (And

Table 4. Excerpt of measured [Fe/H] and [α/Fe] from our coadded spectra. Includes both validation and science coadds, for both bin types.

Bin type	Coadd type	Mask name	Slit list	[Fe/H]	σ[Fe/H]	[α/Fe]	σ[α/Fe]
[Fe/H]	validation	and7a	[117, 063, 094, 004, 108]	−1.63	0.11	0.30	0.13
[Fe/H]	validation	and7a	[007, 076, 083, 071, 068]	−1.43	0.10	0.06	0.12
[Fe/H]	validation	and7a	[124, 000, 062, 067, 065]	−1.17	0.10	0.44	0.14
[Fe/H]	validation	and7a	[047, 123, 075, 049, 026]	−1.39	0.11	0.33	0.13
[Fe/H]	validation	and7a	[034, 020, 011, 090, 058]	−1.43	0.11	0.30	0.14
[Fe/H]	validation	and7a	[073, 091, 060, 125, 061]	−1.66	0.10	0.12	0.12
[Fe/H]	science	and7a	[040, 010, 029, 059, 015, 084, 054, 112, 107]	−1.77	0.11	−0.26	0.16
[Fe/H]	science	and7a	[066, 113, 120, 086, 081]	−1.70	0.12	0.40	0.20
[Fe/H]	science	and7a	[074, 019, 023, 082, 069]	−1.57	0.14	−0.10	0.33
[Fe/H]	science	and7a	[043, 110, 111, 085, 016]	−1.49	0.12	0.18	0.20
[Fe/H]	science	and7a	[051, 018, 025, 012, 024]	−1.57	0.11	−0.35	0.18

NOTE—This table is available in its entirety in machine-readable form.

XVIII, XV, XIV, and IX), our [α/Fe] measurements are the first available for these dwarf galaxies.

For the majority of the dSphs in our sample, we also see a clear decrease in [α/Fe] as a function of [Fe/H] for individual stars (transparent grey points). Even where we have a significantly smaller sample of stars (e.g., And XIV, And X), there is still a visibly negative trend, which is further supported by the inclusion of our coadded abundances. We quantify these trends in Section 7.2. The validation coadd abundance measurements (circles) generally fall neatly within the center of the 2D [α/Fe]–[Fe/H] distribution of the individual stellar abundances, while the science coadded measurements have a wider spread in both [Fe/H] and [α/Fe]. This echoes what we have already found in Figure 8 and with the statistical tests performed in Section 6: the distributions of the validation sample and coadded measurements for a given dSph generally have the same mean, but differing variance.

Vargas et al. (2014a) measured [α/Fe] and [Fe/H] for individual stars in six of the dSphs in our sample (And I, II, III, V, VII, X), and so here we qualitatively compare our results with those presented in their Figure 4. We note that they did not cull their sample to remove stars with large uncertainties, where we have an uncertainty cut at 0.4 dex in both [α/Fe] and [Fe/H] for individual stars in our sample. In addition, they required that spectra in their sample have a minimum S/N of 15 Å^{-1}, while we have no minimum S/N requirement for stars in our sample. Finally, their sample consists of stars from slitmasks with shallow observations only. We find general agreement in the [α/Fe]–[Fe/H] distributions for the dSphs in common between our samples, with one no-

table exception. Vargas et al. (2014a) found a significant plateau in [α/Fe] for the metal-rich ([Fe/H]>∼ −1.5 dex) stars in And VII. In contrast, we find that while we have a number of high-[α/Fe], metal-rich stars in And VII, they do not form a plateau. However, we note that while we measure a negative trend in the individual stars (Section 7.2), we do not measure a significant negative trend with our coadded measurements.

7.2. Star formation history of M31 dSphs from coadded spectra

In Section 7, we presented [Fe/H] and [α/Fe] for ten dSphs in M31, nine of which have at least one measurement from individual stars, and all have coadded measurements that are representative of the distribution of individual abundance measurements. Five of these dSphs were also presented by Kirby et al. (2020): And VII, And I, And III, And V, and And X, where in addition to atmospheric [α/Fe], they also measure individual α-elements (Mg, Ca, Si, Ti) for a number of stars in their sample with sufficiently high S/N. In this section, we will focus on the star formation history (SFH) from coadded measurements in M31 dSphs at the lower end of the mass range of our sample (And V - And X), as significant discussion of SFH of the higher mass dSphs (And VII, II, I, and III) based on this chemical space were discussed at length in previous works (e.g. Kirby et al. 2020; Vargas et al. 2014a).

Vargas et al. (2014a) used the [α/Fe]–[Fe/H] plane to characterize the SFHs of the dSphs in their sample, and compared their results to those in the literature from photometric studies of their CMDs (e.g., Grebel & Guhathakurta 1999; da Costa et al. 2000; Da Costa et al.
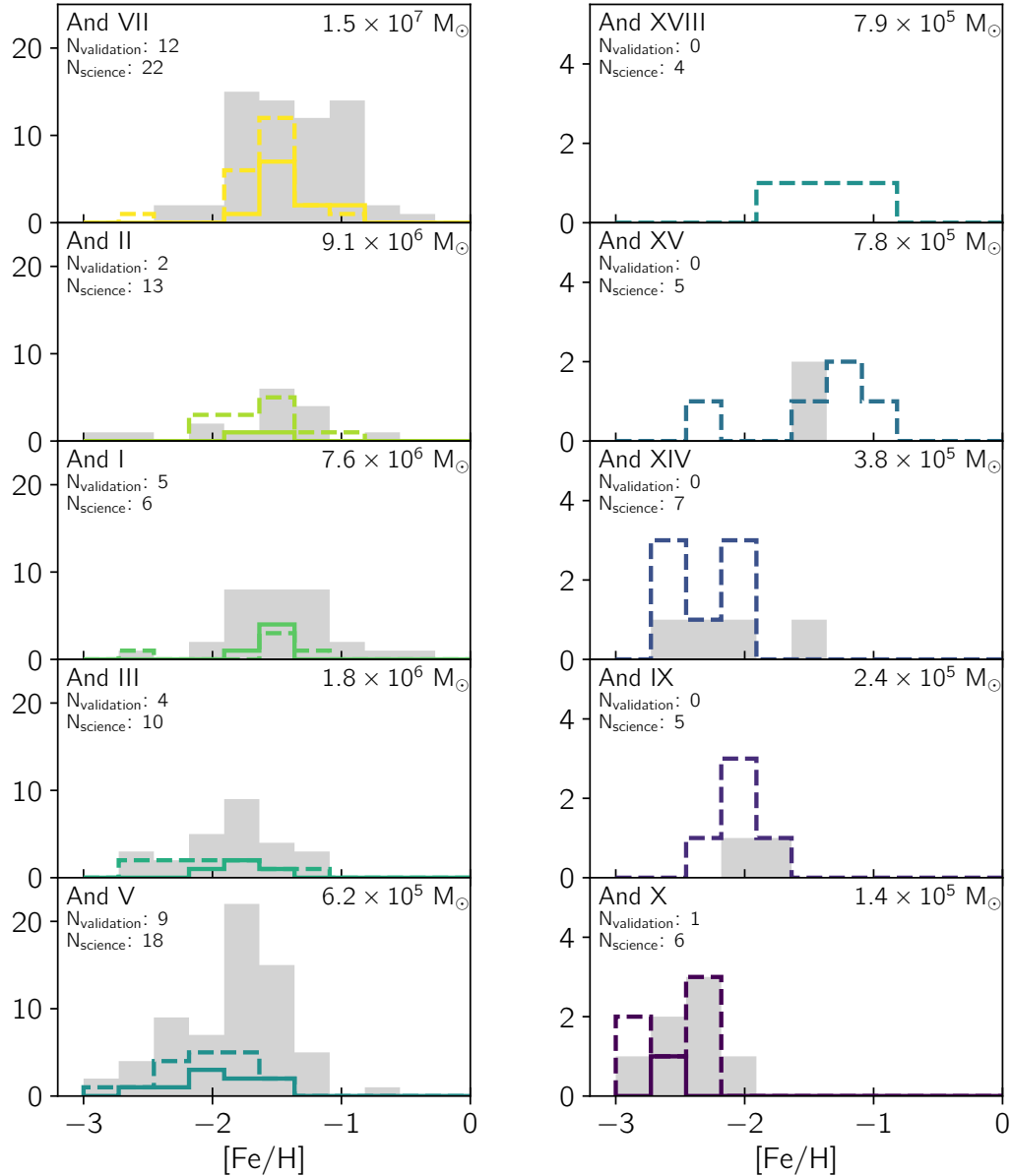
Figure 8. [Fe/H] distributions for our ten M31 dSphs roughly ordered from most massive to least massive (left column, top to bottom, then right column, top to bottom). The filled grey histogram represents the individual [Fe/H] measurements from both shallow and deep (low and high S/N) data. The colored histograms represent the measurements made from coadded spectra, where the solid line denotes the validation coadds, and the dashed line indicates the science coadds. The stellar mass of each dSph is indicated in its respective panel.

2002; McConnachie et al. 2007; Weisz et al. 2014). To summarize the findings from photometric studies: the majority of M31 dSphs show evidence for an extended SFH from their CMDs, with prominent red horizontal branch (HB) stars. The presence of a red HB indicates stars that formed more recently at multiple metallicities, compared to the primarily metal-poor, ancient stars that populate the blue HB. Martin et al. (2017) reached sim-

ilar conclusions for some of the less massive satellites (And XVIII, XV, IX, X) in our sample.

We find that our coadded measurements follow the same decreasing [α/Fe] with [Fe/H] trend seen in individual stars. The more massive satellites in our sample (left column of Figure 9) illustrate this trend clearly, while the less massive satellites generally exhibit negative trends, albeit with smaller sample sizes. In general, a decreasing trend in [α/Fe] as a function of [Fe/H] in-

Table 5. Coadds from stars with large uncertainties on their individual abundance measurements (science coadds).

Object name	Mask name	N_{stars}	$N_{science\,coadds}$
And I	and1a	10	2
	d1_1	10	2
	d1_2	14	2
And II	d2_1	37	7
	d2_2	34	6
And III	and3a	11	2
	d3_1	20	4
	d3_2	12	2
	d3_3	10	2
And V	and5a	18	3
	and5b	22	4
	d5_1	20	4
	d5_2	24	4
	d5_3	18	3
And VII	and7a	29	5
	d7_1	50	10
	d7_2	36	7
	d7_3	17	3
And IX	d9_1	19	3
	d9_2	10	2
And X	and10a	10	2
	and10b	6	1
	d10_1	7	1
	d10_2	11	2
And XIV	A170_1	12	2
	A170_2	24	4
	d14_3	8	1
And XV	d15_1	16	3
	d15_2	10	2
And XVIII	d18_1	20	4

dicates an extended SFH, which is consistent with what has been inferred from the presence of red HB stars in their CMDs.

We quantitatively investigate the SFHs from coadded measurements in our dSphs by measuring the slope in $[\alpha/\mathrm{Fe}]$–$[\mathrm{Fe/H}]$ space ($d[\alpha/\mathrm{Fe}]/d[\mathrm{Fe/H}]$), where $[\alpha/\mathrm{Fe}]$ acts as a proxy for stellar age, and $[\mathrm{Fe/H}]$ provides a measure of the chemical enrichment. To measure $d[\alpha/\mathrm{Fe}]/d[\mathrm{Fe/H}]$, we use a marginalized posterior distribution with flat priors to fit a line to data with uncertainties on both the dependent and independent axes, presented by Hogg et al. (2010) and described in detail for a similar application in Kirby et al. (2019).

We use a Markov Chain Monte Carlo (MCMC), implemented with the emcee Python package (Foreman-

Mackey et al. 2013), to generate a distribution of models which fit our data while also taking uncertainties into account. Rather than fitting a line with a slope (m) and intercept (b), we parameterize the line of best fit with an angle (θ), and the perpendicular distance of the line from the origin ($b_\perp$), where $b_\perp \equiv b\,cos(\theta)$ (Hogg et al. 2010). This parameterization avoids the preference for shallow slopes when there is a flat prior on the slope. The log likelihood is defined as:

$$\ln \mathscr{L} = -0.5 \sum_{i=1}^{N} \frac{\Delta_i^2}{\Sigma_i^2} - \ln(\sqrt{2\pi}\Sigma_i) \qquad (11)$$

$$\Delta_i = [\alpha/\mathrm{Fe}]_i \cos\theta - [\mathrm{Fe/H}]_i \sin\theta - b_\perp \qquad (12)$$

$$\Sigma_i^2 = \delta[\alpha/\mathrm{Fe}]_i^2 \cos^2\theta + \delta[\mathrm{Fe/H}]_i^2 \sin^2\theta \qquad (13)$$

where for star i, $\delta[\mathrm{Fe/H}]_i$ and $\delta[\alpha/\mathrm{Fe}]_i$ represent the total measurement uncertainties for $[\mathrm{Fe/H}]$ and $[\alpha/\mathrm{Fe}]$, respectively. Using the emcee package, we sample the probability distribution, and transform our parameters back into the more familiar m and b using $m = \tan(\theta)$ and $b = b_\perp/\cos(\theta)$. For both θ and $b_\perp$ we take the median of the resulting distribution as our measured value, and the 16th and 84th percentiles (1σ) as the uncertainties on our measured values.

We measure slopes for both the individual measurements (transparent grey points in Figure 9), as well as the slope for all validation and science coadds combined. The measured slopes and their associated uncertainties are given in Table 6. We find that for the majority of our sample, the slopes from measured individual abundance measurements and coadds roughly agree, within ~ 1 - 2σ. We interpret this finding as another indication that, in general, abundance measurements from our coadded spectra are representative of the overall abundance measurements from individual spectra.

We find evidence for slopes in $[\alpha/\mathrm{Fe}]-[\mathrm{Fe/H}]$ from our coadded measurements at the 2σ significance level for all of our low-mass galaxies with the exception of And VII, And IX, and And XVIII. For And VII, we interpret this as a consequence of the presence of metal-rich, high-$[\alpha/\mathrm{Fe}]$ stars, which would flatten a negative trend in $[\alpha/\mathrm{Fe}]-[\mathrm{Fe/H}]$. Such metal-rich, high-$[\alpha/\mathrm{Fe}]$ stars are absent from our And IX sample, and we discuss below potential reasons for a lack of a significant trend for this dSph. Finally, we note that the slope for And XVIII was measured using only four coadded points.

For our stars in And VII with individual measurements, we find a negative slope in $d[\alpha/\mathrm{Fe}]/d[\mathrm{Fe/H}]$ that roughly corresponds with that found by Kirby et al. (2020), and this negative slope is significantly more shallow compared to other galaxies in the sample. Moreover,
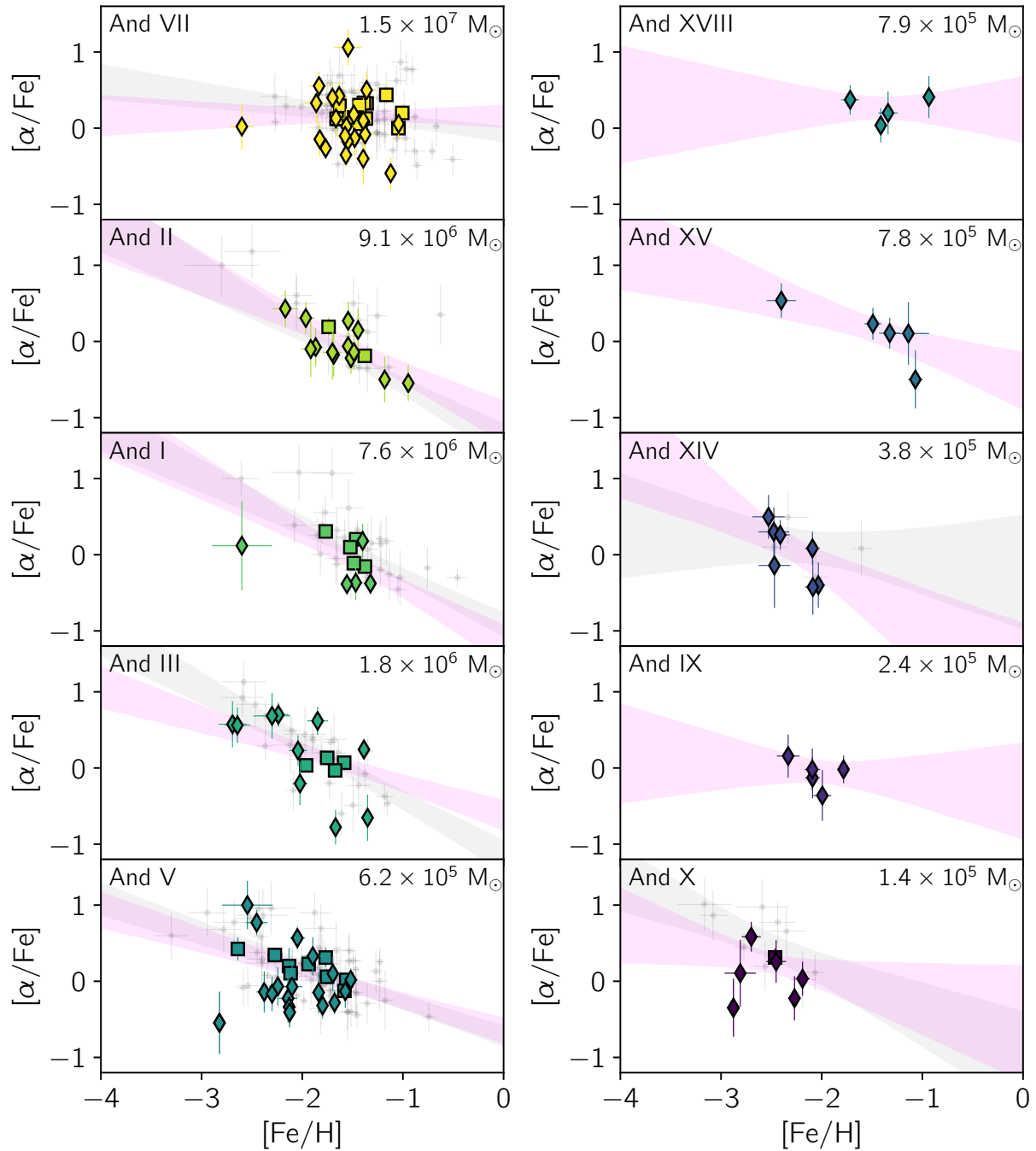
Figure 9. [Fe/H] vs [α/Fe] for our ten M31 dSphs, ordered from most massive to least massive. Small grey circles indicate abundance measurements of individual stars. Square symbols show validation coadds, and diamond symbols indicate science coadds. Fitted slopes and their corresponding 1σ uncertainties measured from individual measurements are shown in grey, and the slopes from all coadds (validation and science combined) for a given dSph are shown in magenta.

using our coadded measurements, we do not find evidence for a negative correlation. These findings, along with the presence of high-$[\alpha/\mathrm{Fe}]$, metal-rich stars is in contrast to the SFH from shallow HST photometry (Weisz et al. 2014), where they find And VII to have an ancient SFH. To resolve this disparity, deeper spectroscopic observations of And VII are needed, as noted by Kirby et al. (2020).

The slopes that we measure quantitatively agree with Kirby et al. (2020), where the shallower slopes of the more massive galaxies indicate higher star formation rates over an extended period. They compare the observed metallicity distribution function (MDF) with chemical evolution models (Kirby 2011; Kirby et al. 2013) to find a best fit chemical evolution model, and compare these best fit models with the slopes they measure in $[\alpha/\mathrm{Fe}]$–$[\mathrm{Fe/H}]$. They find that galaxies with shallower slopes are incompatible with a simple Leaky Box Model (Schmidt 1963; Talbot & Arnett 1971), and are more suggestive of the Pre-Enriched Model (Pagel 1997), or a model where gas accretion prolongs star formation (Accretion Model, Lynden-Bell 1975). In the Leaky Box model, a galaxy can lose gas at the same rate of its star formation, but does not acquire any new gas. The fact that we find more massive galaxies to have shallower slopes in $[\alpha/\mathrm{Fe}]$–$[\mathrm{Fe/H}]$ indicates they are more likely to hold on to their gas, or have had some accretion of gas, likely owing to the depth of their gravitational potential wells (in comparison to the less massive dSphs) (Tolstoy et al. 2009; Letarte et al. 2010; Kirby 2011). As a result, these galaxies have a less efficient SFH, where Type Ia supernovae, which produce more Fe than α elements, dominate over Type II supernovae.

We take the presence of a slope in our lower mass galaxies as further evidence of an extended star formation history in these galaxies, as also evidenced by the presence of red HB stars in the CMDs. And XIV in particular is interesting because it hosts a more balanced (i.e., a more equal number of red HB and blue HB stars) HB (Martin et al. 2017) in comparison to the other dSphs in the low-mass regime. From our spectroscopic abundance measurements, we find that it is more metal-poor than one would naively expect following the mass-metallicity relation (MZR, Section 7.3). These spectroscopic measurements corroborate the evidence from photometric data that And XIV hosts a more substantial fraction of old, metal-poor stars in comparison to other dSphs of similar mass.

We also find tentative evidence for a slope in the $[\alpha/\mathrm{Fe}]$–$[\mathrm{Fe/H}]$ distribution for And IX ($m = -0.12 \pm 0.10$). Using HST photometry, Martin et al. (2017) found And IX was relatively metal-rich for its stellar mass, but they noted that their sample likely had some contamination from the M31 halo. Such contamination would affect the slope by making it more flat. However, even considering our strict membership criteria, we still find that And IX is more metal-rich than other dSphs of similar mass. We note that the slope $(d[\alpha/\mathrm{Fe}]/d[\mathrm{Fe/H}])$ we measure from coadded stars in And IX is significantly shallower compared to other dSphs with similar stellar masses. This difference in the slope may be due to the presence of metal-rich stars (which are undetected in our sample of And IX stars, unlike for And VII), large uncertainties in $[\alpha/\mathrm{Fe}]$, or simply a lack of spectroscopic metallicity measurements at the metal-poor end of the distribution. As the slope from coadded measurements is calculated from only five stars, we refrain from drawing further conclusions.

7.3. The mass-metallicity relation

Kirby et al. (2013) presented a mass-metallicity relation (MZR) for dwarf galaxies in the Local Group, fit using 15 MW dSphs. In their analysis, they found from coadded spectra that the M31 dSphs in their sample roughly corresponded to the same relation, indicating that satellite galaxies of the MW and M31 share the same MZR, which is roughly consistent with the MZR measured from more massive galaxies. However, for the majority of their M31 dSphs, the average metallicity was calculated by coadding stars in only a few bins, and in some cases, only one bin was used for a given dSph. Kirby et al. (2020) update this result by remeasuring the mean $[\mathrm{Fe/H}]$ from measurements from individual stars for five M31 dSphs with deep spectroscopic observations (And I, III, V, VII, X). They find that their new values agree within 0.2 dex for all dSphs in their sample except for And VII, which agrees within 0.25 dex.

We update this finding by combining both the individual measurements and the coadded measurements for $[\mathrm{Fe/H}]$ for each dSph. To do this, we take the uncertainty-weighted average of the individual and coadded measurements, where the total uncertainty for individual stars is given in Section 3.3.4, and the total uncertainty for our coadded measurements is given by Eq. 5. Stellar mass and mean $[\mathrm{Fe/H}]$ are given in Table 6 for each dSph in our sample. Stellar masses for M31 dSphs are the same as in Kirby et al. (2020) and Kirby et al. (2013), where the mass-to-light ratios from Woo et al. (2008) are multiplied by luminosities presented in Tollerud et al. (2012) and McConnachie (2012).

Figure 10 shows the MZR from our sample of M31 dSphs, compared to the values from Kirby et al. (2013) and Kirby et al. (2020). Overall, we find that our measurements (black triangles) are consistent with the mean
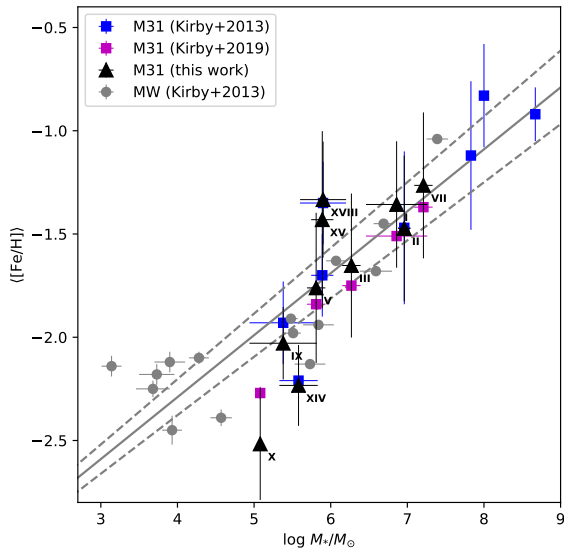
Figure 10. Mass-metallicity relation for Local Group satellites. Average metallicities measured with individual stars in MW dSphs from Kirby et al. (2013) are indicated with grey circles, average metallicities measured from coadded spectra for M31 dSphs from Kirby et al. (2013) are indicated with blue squares, and average metallicities measured from individual stars in M31 dSphs from Kirby et al. (2020) are indicated with purple squares. Our measurements are indicated with black triangles, labelled with the name of the M31 dSph. The solid grey line shows the MZR from Kirby et al. (2013), with the dashed lines indicating 1σ uncertainties, fit using MW dSphs only. The average metallicity of M31 dSphs, whether measured from individual or coadded spectra, fit this relation.

[Fe/H] from either coadded measurements (Kirby et al. 2013) or individual measurements (Kirby et al. 2020). We note that while And X and XIV seem to deviate from the MZR fit from MW dSphs, our measurements are consistent within $\sim 1-2\sigma$ uncertainty. Using our updated sample, which includes coadded abundances from stars that did not have high enough S/N to derive individual measurements, we demonstrate that we can robustly determine the average metallicity of a given M31 dSph by properly accounting for these stars.

8. CONCLUSIONS

We present a coaddition method for DEIMOS spectra of red giant branch stars in M31's dwarf spheroidal galaxies. We validate our method using high quality data that cover a range of S/N regimes: MW globular clusters (high S/N), M31 dSphs with deep observations (lower S/N), and M31 dSphs with shallow observations (lowest S/N).

For both our validation coadds and science coadds, we include only stars that are known members of a given object (either GC or dSph), selected using their radial velocities, position on the CMD, and spectral features. We show that we can accurately reproduce the weighted average [Fe/H] and [α/Fe] of coadded spectra, where similar stars grouped by either photometric temperature ($T_{\rm eff}$) or metallicity ([Fe/H]). We find no significant differences in the results with either binning method, and we choose to present the measurements binned by photometric [Fe/H]. Using validation coadds, we characterize the systematic uncertainties of our coadded measurements, and we find that the systematic uncertainty limit that we adopt from Kirby et al. (2010) is sufficient.

We then coadd all of the member stars in our M31 dSph slitmasks that did not pass the quality criteria, i.e., they have large uncertainties, they hit the edge of the spectral synthesis grid during the continuum refinement step, or in the continuum refinement did not converge. We compare the science coadds to both the 1D ([Fe/H]) and 2D ([α/Fe]–[Fe/H]) abundance distributions from measurements of individual stars, and find that they agree. In [α/Fe]–[Fe/H] space, we find that our science coadds follow the same trend of decreasing [α/Fe] with increasing [Fe/H], allowing us to fit slopes to these trends.

For four of the dSphs in our sample (And XVIII, XV, XIV, IX), we present the first [α/Fe] measurements available. These galaxies, which are less massive and have fewer member stars than the rest of our sample, still show the same general trend of decreasing average metallicity as a function of stellar mass. In addition, there is some indication that these dSphs exhibit the same declining [α/Fe]-[Fe/H] trends that we find in the more massive dSphs. This trend indicates an extended star formation history for these less massive dSphs, consistent with what has been found via photometric studies.

Finally, we use our validation sample as well as our coadds to measure the average metallicity ([Fe/H]) of a dwarf galaxy as a function of mass. For four galaxies in our sample (And IX, XIV, XV, XVIII), these measurements are updated from the values presented in Kirby et al. (2013), and agree within 1σ. We also compare our values measured from combined coadded and individual measurements with those presented in Kirby et al. (2020), measured using only individual measurements. Again, we find them to agree within 1σ (~ 0.2 dex). We conclude that we can robustly determine average [Fe/H] for the dSphs in our sample, using combined coadded and individual measurements.

Table 6. Mass-metallicity Relation and Abundance Trends in M31 dSphs.

Object name	$\log(\mathrm{M_*/M_\odot})$	$\langle[\mathrm{Fe/H}]\rangle$	m (individual)	m (coadd)
And VII	$7.21 \pm 0.12^*$	-1.26 ± 0.003	-0.17 ± 0.07	$+0.01 \pm 0.09$
And II	6.96 ± 0.08	-1.47 ± 0.006	-0.72 ± 0.14	-0.64 ± 0.16
And I	$6.86 \pm 0.40^*$	-1.36 ± 0.004	-0.65 ± 0.10	-0.73 ± 0.15
And III	$6.27 \pm 0.12^*$	-1.65 ± 0.005	-0.73 ± 0.11	-0.42 ± 0.10
And V	$5.81 \pm 0.12^*$	-1.76 ± 0.003	-0.45 ± 0.06	-0.40 ± 0.08
And XVIII	5.90 ± 0.30	-1.33 ± 0.02	...	-0.01 ± 0.25
And XV	5.89 ± 0.145	-1.43 ± 0.42	...	-0.43 ± 0.21
And XIV	5.58 ± 0.25	-2.23 ± 0.01	-0.16 ± 0.29	-0.80 ± 0.82
And IX	5.38 ± 0.44	-2.03 ± 0.01	...	-0.12 ± 0.26
And X	$5.08 \pm 0.03^*$	-2.52 ± 0.27	-0.60 ± 0.21	-0.32 ± 0.25

NOTE—Masses indicated with asterisks are from Kirby et al. (2020), and are the product of the stellar mass-to-light ratios from Woo et al. (2008) and luminosities from Tollerud et al. (2012). Masses without asterisks are from (Kirby et al. 2013) and references therein.

In future work, we plan to apply this coaddition method to stars across a number of M31 halo fields. These fields are too sparsely populated by member stars with high enough S/N to measure their abundances individually, but with our coaddition method, we will be able to measure average spectroscopic metallicities across the M31 halo. This will allow us to compare the metallicity, and therefore formation history, of the smooth halo compared to its rich substructure.

REFERENCES

Adelman-McCarthy, J. K., Agüeros, M. A., Allam, S. S., et al. 2006, ApJS, 162, 38, doi: 10.1086/497917

Arnett, D. 1996, Supernovae and nucleosynthesis. an
    investigation of the history of matter, from the Big Bang
    to the present

Astropy Collaboration, Robitaille, T. P., Tollerud, E. J.,
    et al. 2013, A&A, 558, A33,
    doi: 10.1051/0004-6361/201322068

Astropy Collaboration, Price-Whelan, A. M., Sipőcz, B. M.,
    et al. 2018, AJ, 156, 123, doi: 10.3847/1538-3881/aabc4f

Beaton, R. L. 2014, PhD thesis, University of Virginia

Boeche, C., Siebert, A., Piffl, T., et al. 2013, A&A, 559,
    A59, doi: 10.1051/0004-6361/201322085

Bullock, J. S., & Johnston, K. V. 2005, ApJ, 635, 931,
    doi: 10.1086/497422

Carollo, D., Beers, T. C., Lee, Y. S., et al. 2007, Nature,
    450, 1020, doi: 10.1038/nature06460

Castelli, F., Gratton, R. G., & Kurucz, R. L. 1997, A&A,
    318, 841

Collins, M. L. M., Chapman, S. C., Rich, R. M., et al. 2011,
    MNRAS, 417, 1170,
    doi: 10.1111/j.1365-2966.2011.19342.x

Collins, M. L. M., Chapman, S. C., Rich, R. M., et al. 2013,
    ApJ, 768, 172, doi: 10.1088/0004-637X/768/2/172

Cooper, A. P., Cole, S., Frenk, C. S., et al. 2010, MNRAS,
    406, 744, doi: 10.1111/j.1365-2966.2010.16740.x

Cooper, M. C., Newman, J. A., Davis, M., Finkbeiner,
    D. P., & Gerke, B. F. 2012, spec2d: DEEP2 DEIMOS
    Spectral Pipeline, Astrophysics Source Code Library.
    http://ascl.net/1203.003

Da Costa, G. S., Armandroff, T. E., & Caldwell, N. 2002,
    AJ, 124, 332, doi: 10.1086/340965

da Costa, L. N., Bernardi, M., Alonso, M. V., et al. 2000,
    AJ, 120, 95, doi: 10.1086/301449

Demarque, P., Woo, J.-H., Kim, Y.-C., & Yi, S. K. 2004,
    ApJS, 155, 667, doi: 10.1086/424966

Dorman, C. E., Guhathakurta, P., Fardal, M. A., et al.
    2012, ApJ, 752, 147, doi: 10.1088/0004-637X/752/2/147

Dorman, C. E., Guhathakurta, P., Seth, A. C., et al. 2015,
    ApJ, 803, 24, doi: 10.1088/0004-637X/803/1/24

Escala, I., Gilbert, K. M., Kirby, E. N., et al. 2019a, arXiv
    e-prints, arXiv:1909.00006.
    https://arxiv.org/abs/1909.00006

Escala, I., Kirby, E. N., Gilbert, K. M., Cunningham,
    E. C., & Wojno, J. 2019b, ApJ, 878, 42,
    doi: 10.3847/1538-4357/ab1eac

Faber, S. M., Phillips, A. C., Kibrick, R. I., et al. 2003, in
    Proc. SPIE, Vol. 4841, Instrument Design and
    Performance for Optical/Infrared Ground-based
    Telescopes, ed. M. Iye & A. F. M. Moorwood, 1657–1669,
    doi: 10.1117/12.460346

Font, A. S., McCarthy, I. G., Crain, R. A., et al. 2011,
    MNRAS, 416, 2802,
    doi: 10.1111/j.1365-2966.2011.19227.x

Foreman-Mackey, D., Hogg, D. W., Lang, D., & Goodman,
    J. 2013, PASP, 125, 306, doi: 10.1086/670067

Gilbert, K. M., Kirby, E. N., Escala, I., et al. 2019, ApJ,
    883, 128, doi: 10.3847/1538-4357/ab3807

Gilbert, K. M., Guhathakurta, P., Kalirai, J. S., et al. 2006,
    ApJ, 652, 1188, doi: 10.1086/508643

Gilbert, K. M., Guhathakurta, P., Beaton, R. L., et al.
    2012, ApJ, 760, 76, doi: 10.1088/0004-637X/760/1/76

Gilbert, K. M., Kalirai, J. S., Guhathakurta, P., et al. 2014,
    ApJ, 796, 76, doi: 10.1088/0004-637X/796/2/76

Gilbert, K. M., Tollerud, E., Beaton, R. L., et al. 2018,
    ApJ, 852, 128, doi: 10.3847/1538-4357/aa9f26

Gilmore, G., & Wyse, R. F. G. 1991, ApJL, 367, L55,
    doi: 10.1086/185930

—. 1998, AJ, 116, 748, doi: 10.1086/300459

Gilmore, G., Wyse, R. F. G., & Norris, J. E. 2002, ApJL,
    574, L39, doi: 10.1086/342363

Girardi, L. 2016, ARA&A, 54, 95,
    doi: 10.1146/annurev-astro-081915-023354

Grebel, E. K., & Guhathakurta, P. 1999, ApJL, 511, L101,
    doi: 10.1086/311852

Guhathakurta, P., Ostheimer, J. C., Gilbert, K. M., et al.
    2005, arXiv e-prints, astro.
    https://arxiv.org/abs/astro-ph/0502366

Guhathakurta, P., Rich, R. M., Reitzel, D. B., et al. 2006,
    AJ, 131, 2497, doi: 10.1086/499562

Hayden, M. R., Bovy, J., Holtzman, J. A., et al. 2015, ApJ,
    808, 132, doi: 10.1088/0004-637X/808/2/132

Helmi, A., Veljanoski, J., Breddels, M. A., Tian, H., &
    Sales, L. V. 2017, A&A, 598, A58,
    doi: 10.1051/0004-6361/201629990

Ho, N., Geha, M., Munoz, R. R., et al. 2012, ApJ, 758, 124,
    doi: 10.1088/0004-637X/758/2/124

Hogg, D. W., Bovy, J., & Lang, D. 2010, arXiv e-prints,
    arXiv:1008.4686.   https://arxiv.org/abs/1008.4686

Hunter, J. D. 2007, Computing in Science and Engineering,
    9, 90, doi: 10.1109/MCSE.2007.55

Ibata, R., Irwin, M., Lewis, G., Ferguson, A. M. N., &
    Tanvir, N. 2001, Nature, 412, 49.
    https://arxiv.org/abs/astro-ph/0107090

Ibata, R. A., Gilmore, G., & Irwin, M. J. 1994, Nature,
    370, 194, doi: 10.1038/370194a0

Ibata, R. A., Lewis, G. F., Conn, A. R., et al. 2013, Nature,
    493, 62, doi: 10.1038/nature11717

Ishigaki, M. N., Chiba, M., & Aoki, W. 2012, ApJ, 753, 64,
    doi: 10.1088/0004-637X/753/1/64

Kalirai, J. S., Gilbert, K. M., Guhathakurta, P., et al. 2006, ApJ, 648, 389, doi: 10.1086/505697

Kalirai, J. S., Zucker, D. B., Guhathakurta, P., et al. 2009, ApJ, 705, 1043, doi: 10.1088/0004-637X/705/1/1043

Kalirai, J. S., Beaton, R. L., Geha, M. C., et al. 2010, ApJ, 711, 671, doi: 10.1088/0004-637X/711/2/671

Kirby, E. N. 2011, PASP, 123, 531, doi: 10.1086/660019

Kirby, E. N., Cohen, J. G., Guhathakurta, P., et al. 2013, ApJ, 779, 102, doi: 10.1088/0004-637X/779/2/102

Kirby, E. N., Gilbert, K. M., Escala, I., et al. 2020, AJ, 159, 46, doi: 10.3847/1538-3881/ab5f0f

Kirby, E. N., Guhathakurta, P., Bolte, M., Sneden, C., & Geha, M. C. 2009, ApJ, 705, 328, doi: 10.1088/0004-637X/705/1/328

Kirby, E. N., Guhathakurta, P., & Sneden, C. 2008, ApJ, 682, 1217, doi: 10.1086/589627

Kirby, E. N., Guhathakurta, P., Zhang, A. J., et al. 2016, ApJ, 819, 135, doi: 10.3847/0004-637X/819/2/135

Kirby, E. N., Simon, J. D., & Cohen, J. G. 2015, ApJ, 810, 56, doi: 10.1088/0004-637X/810/1/56

Kirby, E. N., Guhathakurta, P., Simon, J. D., et al. 2010, ApJS, 191, 352, doi: 10.1088/0067-0049/191/2/352

Kirby, E. N., Xie, J. L., Guo, R., et al. 2019, ApJ, 881, 45, doi: 10.3847/1538-4357/ab2c02

Kordopatis, G., Binney, J., Gilmore, G., et al. 2015, MNRAS, 447, 3526, doi: 10.1093/mnras/stu2726

Kupka, F., Piskunov, N., Ryabchikova, T. A., Stempels, H. C., & Weiss, W. W. 1999, A&AS, 138, 119, doi: 10.1051/aas:1999267

Kurucz, R. L. 1992, RMxAA, 23

—. 1993, Physica Scripta Volume T, 47, 110, doi: 10.1088/0031-8949/1993/T47/017

Letarte, B., Hill, V., Tolstoy, E., et al. 2010, A&A, 523, A17, doi: 10.1051/0004-6361/200913413

Lynden-Bell, D. 1975, Vistas in Astronomy, 19, 299, doi: 10.1016/0083-6656(75)90005-7

Majewski, S. R., Ostheimer, J. C., Kunkel, W. E., & Patterson, R. J. 2000, AJ, 120, 2550, doi: 10.1086/316836

Martin, N. F., Weisz, D. R., Albers, S. M., et al. 2017, ApJ, 850, 16, doi: 10.3847/1538-4357/aa901a

Matteucci, F., ed. 2001, Astrophysics and Space Science Library, Vol. 253, The chemical evolution of the Galaxy, doi: 10.1007/978-94-010-0967-6

McConnachie, A. W. 2012, AJ, 144, 4, doi: 10.1088/0004-6256/144/1/4

McConnachie, A. W., Arimoto, N., & Irwin, M. 2007, MNRAS, 379, 379, doi: 10.1111/j.1365-2966.2007.11969.x

Newman, J. A., Cooper, M. C., Davis, M., et al. 2013, ApJS, 208, 5, doi: 10.1088/0067-0049/208/1/5

Nomoto, K., Iwamoto, K., Nakasato, N., et al. 1997, Nuclear Physics A, 621, 467, doi: 10.1016/S0375-9474(97)00291-1

Ostheimer, James Craig, J. 2003, PhD thesis, UNIVERSITY OF VIRGINIA

Pagel, B. E. J. 1997, Nucleosynthesis and Chemical Evolution of Galaxies, 392

Palma, C., Majewski, S. R., Siegel, M. H., et al. 2003, AJ, 125, 1352, doi: 10.1086/367594

Sbordone, L. 2005, Memorie della Societa Astronomica Italiana Supplementi, 8, 61

Sbordone, L., Bonifacio, P., Castelli, F., & Kurucz, R. L. 2004, Memorie della Societa Astronomica Italiana Supplementi, 5, 93

Schmidt, M. 1963, ApJ, 137, 758, doi: 10.1086/147553

Simon, J. D., & Geha, M. 2007, ApJ, 670, 313, doi: 10.1086/521816

Smecker-Hane, T. A., & Wyse, R. F. G. 1992, AJ, 103, 1621, doi: 10.1086/116175

Sneden, C. A. 1973, PhD thesis, THE UNIVERSITY OF TEXAS AT AUSTIN.

Sohn, S. T., Majewski, S. R., Muñoz, R. R., et al. 2007, ApJ, 663, 960, doi: 10.1086/518302

Talbot, Raymond J., J., & Arnett, W. D. 1971, ApJ, 170, 409, doi: 10.1086/151228

Tinsley, B. M. 1979, ApJ, 229, 1046, doi: 10.1086/157039

—. 1980, FCPh, 5, 287

Tollerud, E. J., Geha, M. C., Vargas, L. C., & Bullock, J. S. 2013, ApJ, 768, 50, doi: 10.1088/0004-637X/768/1/50

Tollerud, E. J., Beaton, R. L., Geha, M. C., et al. 2012, ApJ, 752, 45, doi: 10.1088/0004-637X/752/1/45

Tolstoy, E., Hill, V., & Tosi, M. 2009, ARA&A, 47, 371, doi: 10.1146/annurev-astro-082708-101650

Tully, R. B., Courtois, H. M., Dolphin, A. E., et al. 2013, The Astronomical Journal, 146, 86, doi: 10.1088/0004-6256/146/4/86

van der Walt, S., Colbert, S. C., & Varoquaux, G. 2011, Computing in Science and Engineering, 13, 22, doi: 10.1109/MCSE.2011.37

VandenBerg, D. A., Bergbusch, P. A., & Dowler, P. D. 2006, ApJS, 162, 375, doi: 10.1086/498451

Vargas, L. C., Geha, M., Kirby, E. N., & Simon, J. D. 2013, ApJ, 767, 134, doi: 10.1088/0004-637X/767/2/134

Vargas, L. C., Geha, M. C., & Tollerud, E. J. 2014a, ApJ, 790, 73, doi: 10.1088/0004-637X/790/1/73

Vargas, L. C., Gilbert, K. M., Geha, M., et al. 2014b, ApJL, 797, L2, doi: 10.1088/2041-8205/797/1/L2

Virtanen, P., Gommers, R., Oliphant, T. E., et al. 2019, arXiv e-prints, arXiv:1907.10121. https://arxiv.org/abs/1907.10121

Weisz, D. R., Skillman, E. D., Hidalgo, S. L., et al. 2014,
    ApJ, 789, 24, doi: 10.1088/0004-637X/789/1/24

Woo, J., Courteau, S., & Dekel, A. 2008, MNRAS, 390,
    1453, doi: 10.1111/j.1365-2966.2008.13770.x

Woosley, S., & Janka, T. 2005, Nature Physics, 1, 147,
    doi: 10.1038/nphys172
Yang, L., Kirby, E. N., Guhathakurta, P., Peng, E. W., &
    Cheng, L. 2013, ApJ, 768, 4,
    doi: 10.1088/0004-637X/768/1/4
Zucker, D. B., Kniazev, A. Y., Martínez-Delgado, D., et al.
    2007, ApJL, 659, L21, doi: 10.1086/516748

APPENDIX

A. COMPARISON WITH KIRBY ET AL. FOR ABUNDANCE MEASUREMENTS FROM INDIVIDUAL STARS

Because we use a revised version (Escala et al. 2019b), rewritten in Python, of the pipeline outlined in Kirby et al. (2008), we verify that our results are consistent with those obtained using the IDL version from Kirby et al. (2008). To do this, we recompute [Fe/H] and [α/Fe] for our GC and deep dSph samples using the most up-to-date version of the IDL pipeline. Figures 11 and 12 show the comparison between [Fe/H] and [α/Fe] from both pipelines, and their associated total uncertainties for our sample of MW GCs and M31 dSphs with deep observations. For our GC sample ($N_{\mathrm{stars}} = 196$, Figure 11), we find a median difference of -0.06 ± 0.16 in [Fe/H], and a median difference of -0.01 ± 0.12 in [α/Fe]. The standard deviation for all GCs is 0.08 ± 0.01 and 0.10 ± 0.02 for [Fe/H] and [α/Fe], respectively. To quantify the agreement between the two pipelines, we follow the formalism described in the Appendix of Kirby et al. (2020). We compute the standard deviation of the difference between the pipelines, normalized by their uncertainties, as follows:

$$\mathrm{stddev}\left(\frac{X_{W19} - X_{K08}}{\sqrt{\delta X_{W19}^2 + \delta X_{K08}^2}}\right) \tag{A1}$$

where X is either [Fe/H] or [α/Fe], and δX is the corresponding total uncertainty. For our GCs, we find this value to be 0.51 ± 0.07 for [Fe/H], and 0.55 ± 0.07 for [α/Fe]. A value of 1.0 or less would indicate that the uncertainties completely explain the scatter in the difference, where a value larger than 1.0 indicates an additional source of uncertainty. We conclude that, for GCs, the pipelines agree within their respective uncertainties because the standard deviations from Equation A1 are less than 1.0.

For our M31 dSphs with deep spectroscopic observations ($N_{\mathrm{stars}} = 145$, Figure 12), we find a median difference of -0.06 ± 0.12 for [Fe/H], and 0.00 ± 0.22 for [α/Fe], with a standard deviation of 0.15 ± 0.02 for [Fe/H] and 0.22 ± 0.04 for [α/Fe]. Applying Eq. A1 to our sample of dSphs, we find values of 0.78 ± 0.09 for [Fe/H] and 0.60 ± 0.09 for [α/Fe]. As in the case of the GCs, these values are less than 1.0, and we confirm that the pipelines agree for individual [Fe/H] and [α/Fe] measurements from our dSphs sample.

B. VALIDATION COADDS GROUPED BY PHOTOMETRIC EFFECTIVE TEMPERATURE

In addition to grouping our stars according to their photometric metallicity ([Fe/H]$_{\mathrm{phot}}$), we also grouped our stars according to their photometric effective temperature. We prefer to use the [Fe/H]$_{\mathrm{phot}}$ grouping for our analysis because the spectral synthesis technique that we use can more easily account for a wide range of T_{eff} than [Fe/H] (Yang et al. 2013). By design, we use the values of T_{eff} measured from photometry in constructing the synthetic spectrum (Section 4.4 that our coadded spectrum is compared to. Therefore, our method accounts for a potentially wide range of T_{eff} for a given coadd when binned by [Fe/H].̇The same cannot be said for the T_{eff} binning scenario, where stars with a large range of [Fe/H]$_{\mathrm{phot}}$ may be coadded together, as we fit for [Fe/H].

In Figures 13, 14, and 15, we find qualitatively similar results to those shown in the main text. We find no significant difference between the binning scenarios in either the values of the offsets or dispersion for all three of our samples.

In Figure 16 we show the [Fe/H] distribution for our sample of individual stars, validation coadds, and science coadds, for each of our ten M31 dSphs. We find these distributions to be very similar to those shown in Figure 8, using the [Fe/H]$_{\mathrm{phot}}$ binning scenario. In Figure 17 we show the 2D [α/Fe]-[Fe/H] distribution for our M31 dSphs, again finding similar results as with the coadds binned by [Fe/H]$_{\mathrm{phot}}$. One notable exception is And VII, where there appears to be a stronger correlation between [Fe/H] and [α/Fe] than seen in Figure 9. However, we refrain from drawing any further conclusions from the differences in And VII, as the slope in Figure 17 is predominantly due to only two points (both coadds). As expected, binning by $T_{\mathrm{eff,phot}}$ results in a narrower range of [Fe/H] values compared to binning by [Fe/H]$_{\mathrm{phot}}$. We draw the same conclusion as Yang et al. (2013): both binning scenarios produce abundance distributions that agree within their associated uncertainties. Our decision to use the [Fe/H]$_{\mathrm{phot}}$ is motivated primarily by the desire to limit potential sources of additional systematic uncertainties, as a range of T_{eff} in a given [Fe/H]$_{\mathrm{phot}}$ bin is more easily accounted for in our pipeline.
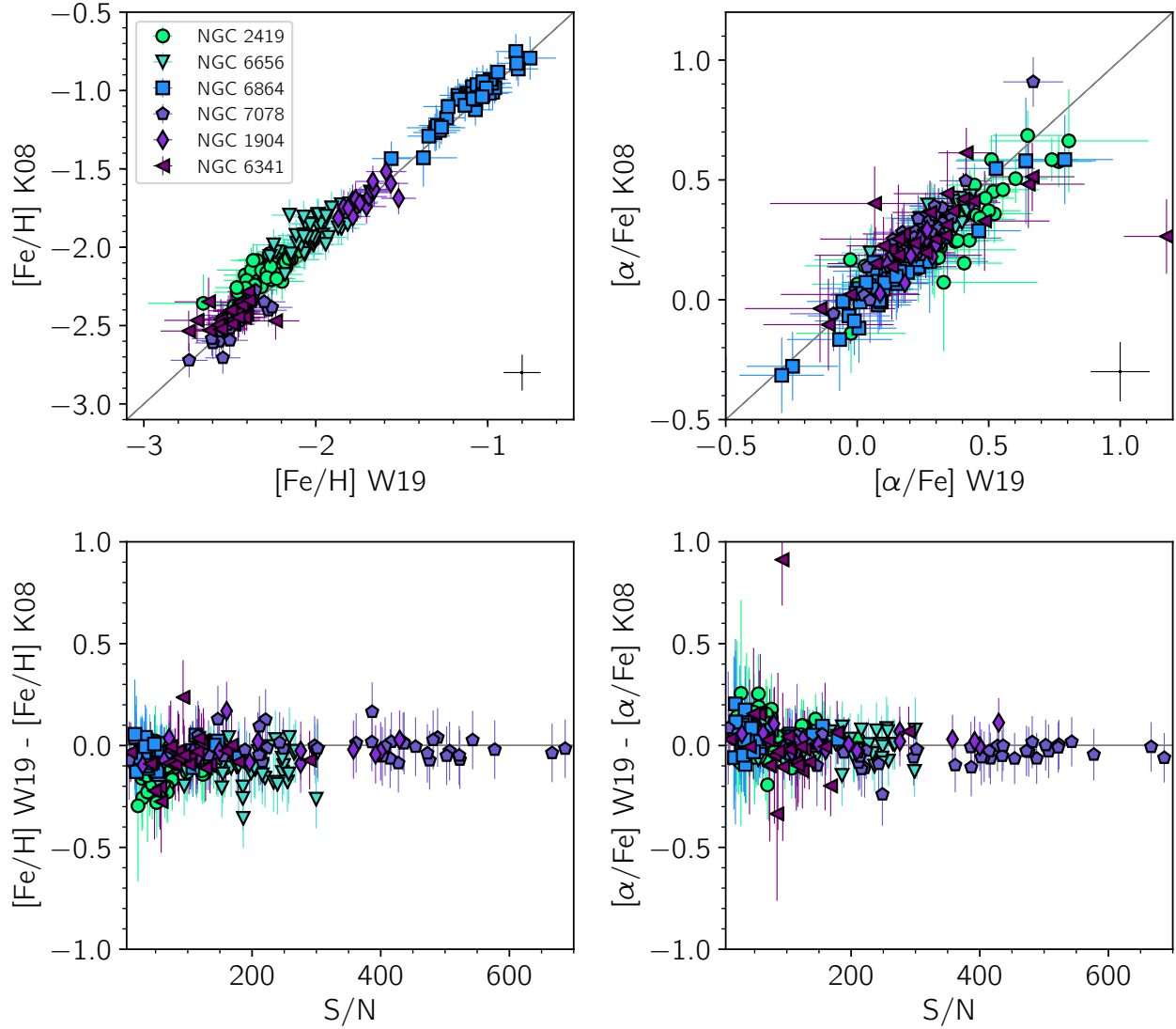
Figure 11. Top row: abundance comparison for all measurements for individual stars in our sample of MW GCs between the pipeline rewritten in Python (Escala et al. 2019b) used for this study (W19), and that used for previous studies, written in IDL (K08, Kirby et al. 2008). The left column shows [Fe/H] and the right column shows [α/Fe] for stars that pass the membership and quality criteria described in Section 4.1. Mean uncertainties are indicated in black for [Fe/H] and [α/Fe] in the left and right panels, respectively. Bottom row: the difference between the two pipelines as a function of S/N. We confirm that the two pipelines generally return similar results within the uncertainties, and the dispersion of the differences decreases as a function of increasing S/N.
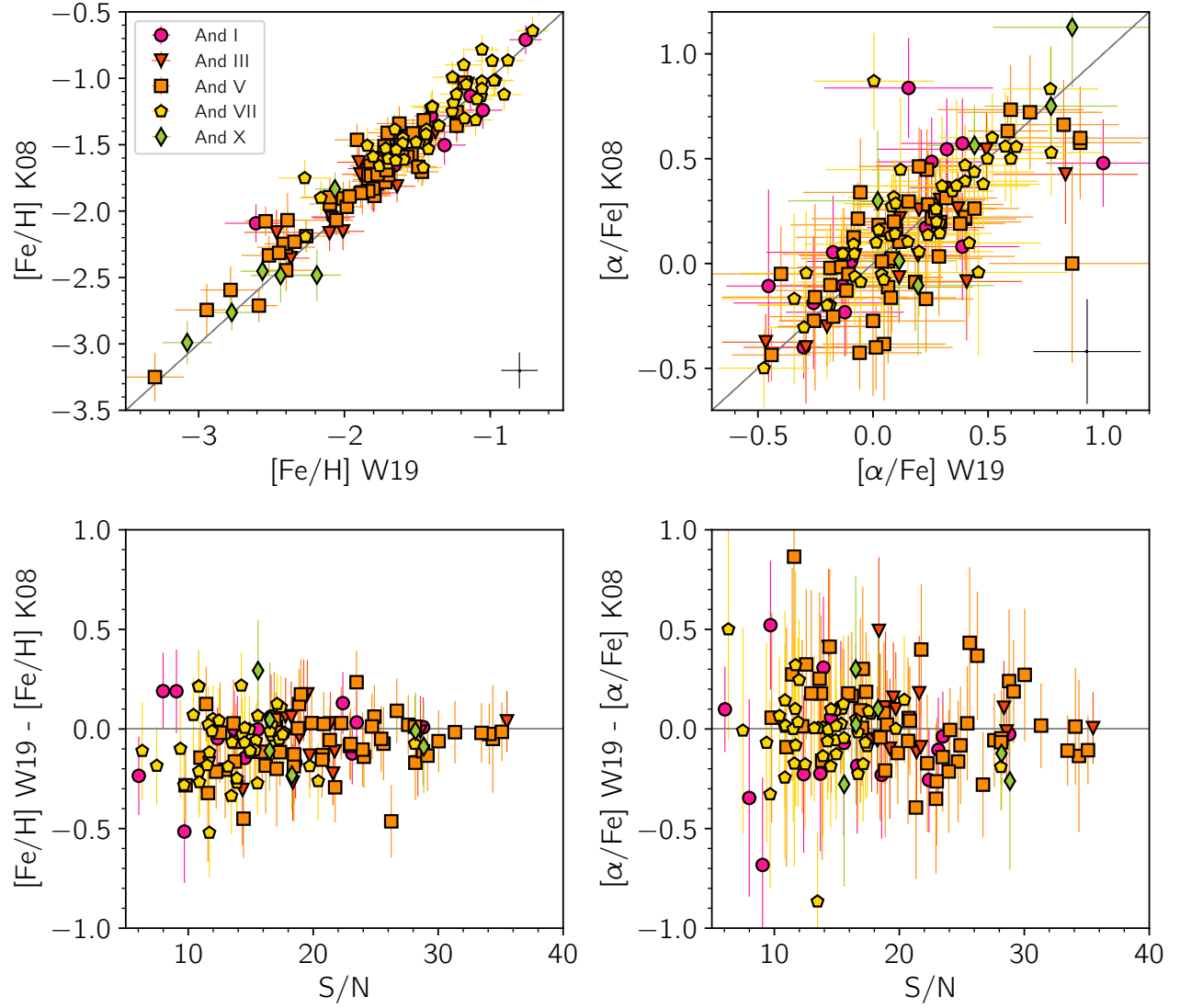
Figure 12. The same as Figure 11, but for our sample of dSphs with deep observations.
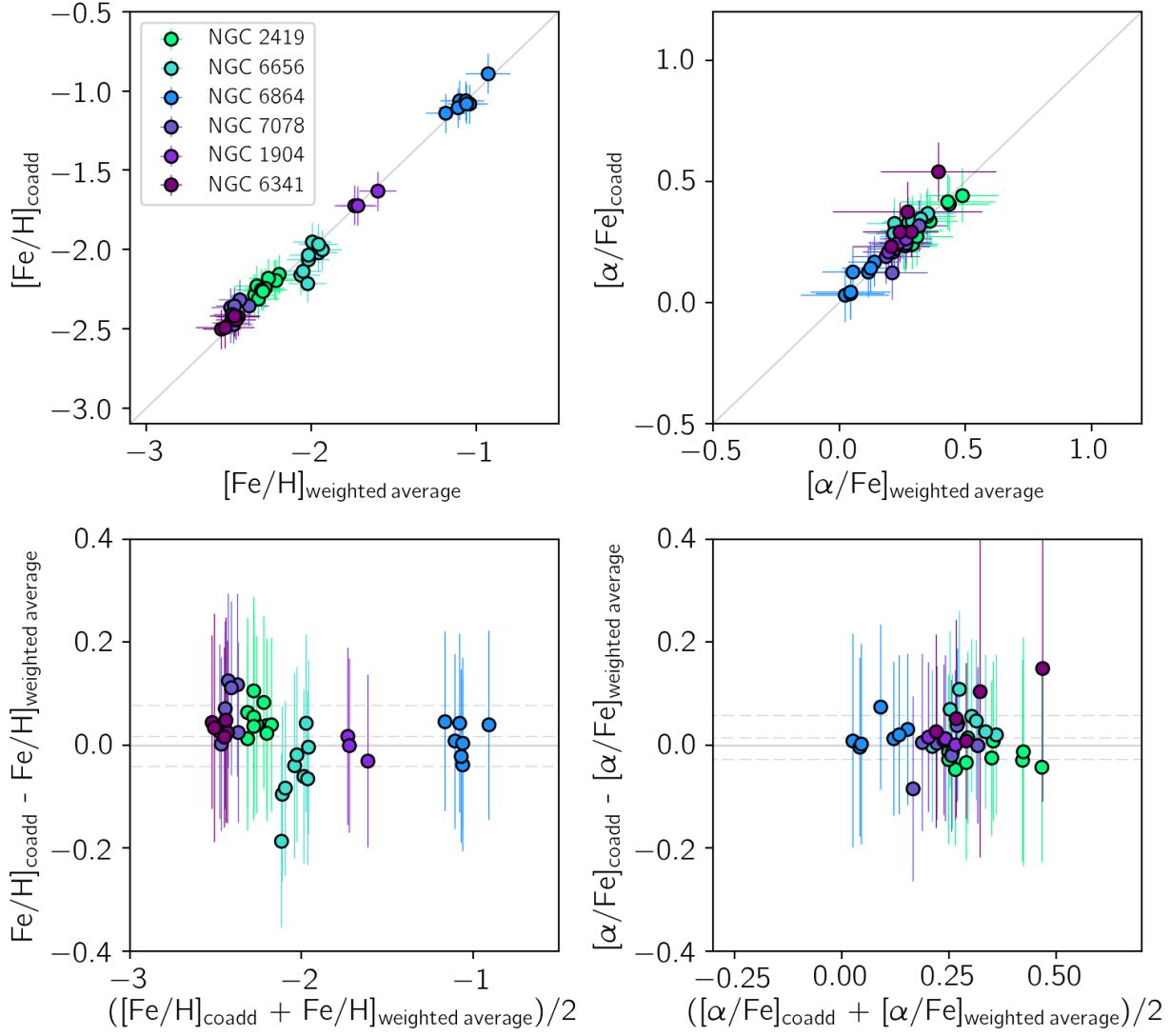
Wojno et al.

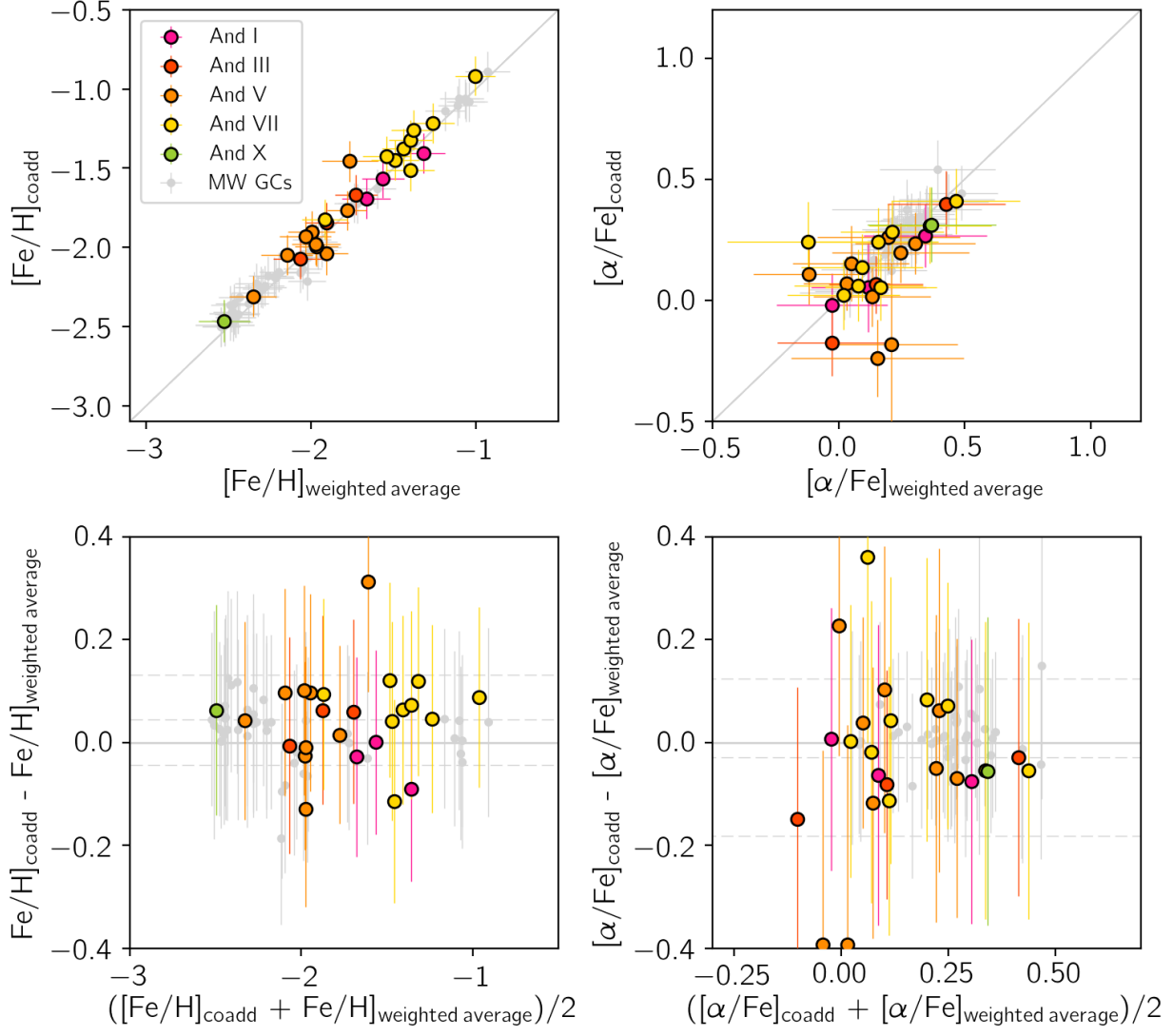**Figure 13.** The same as Figure 5, but for stars binned by $T_{\rm eff}$.

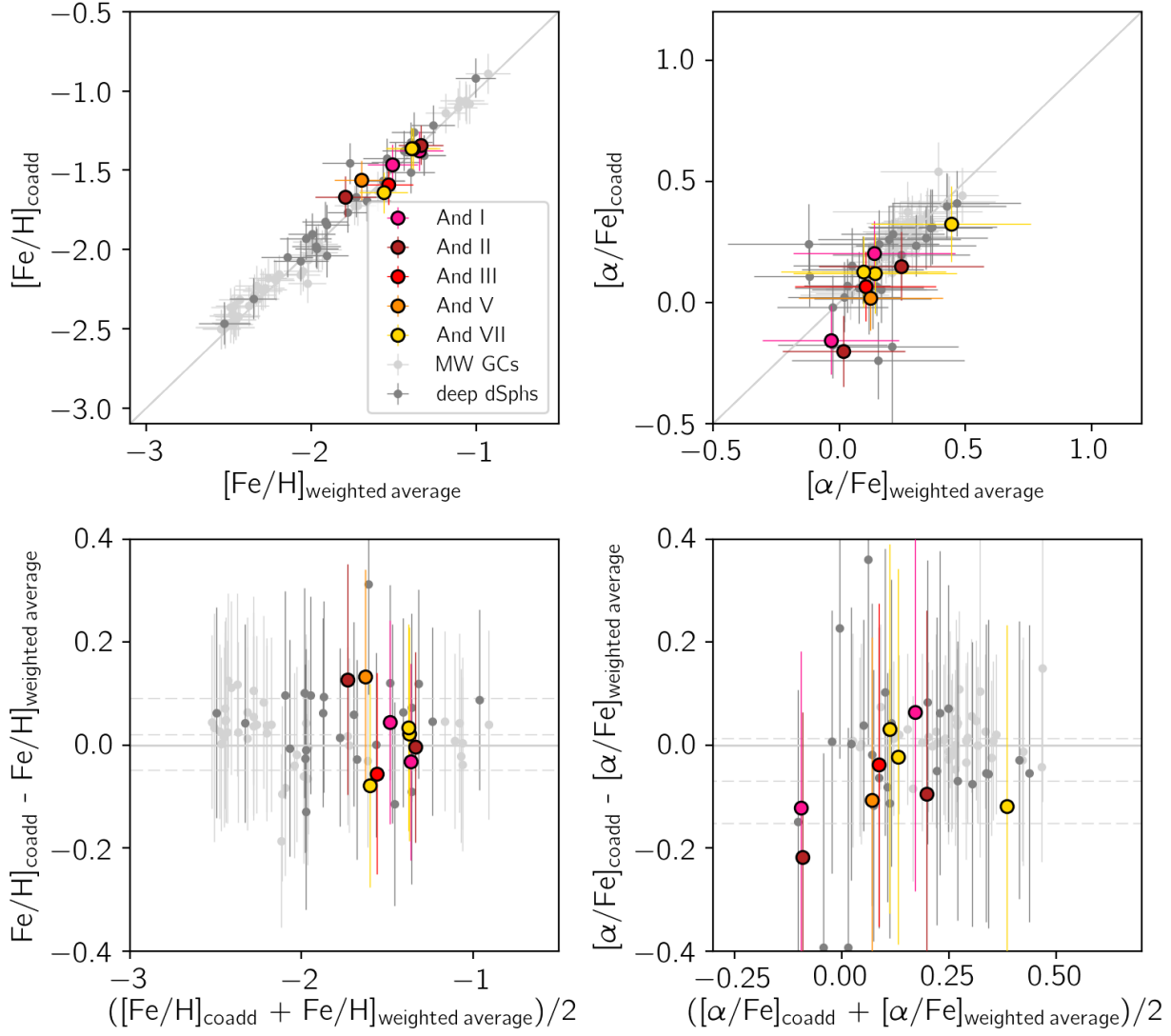**Figure 14.** The same as Figure 6, but for stars binned by $T_{\rm eff}$.

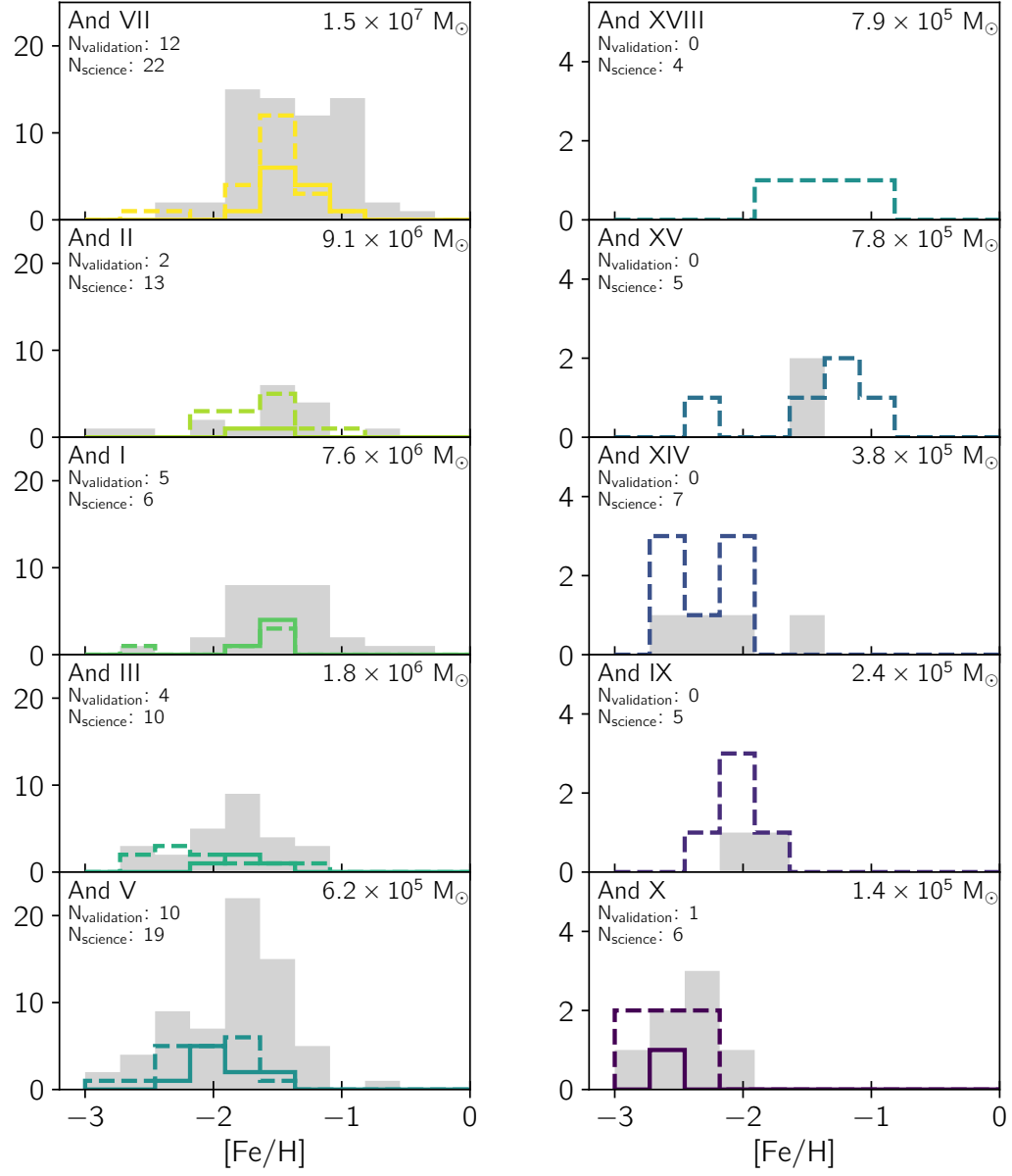**Figure 15.** The same as Figure 7, but for stars binned by $T_{\rm eff}$.

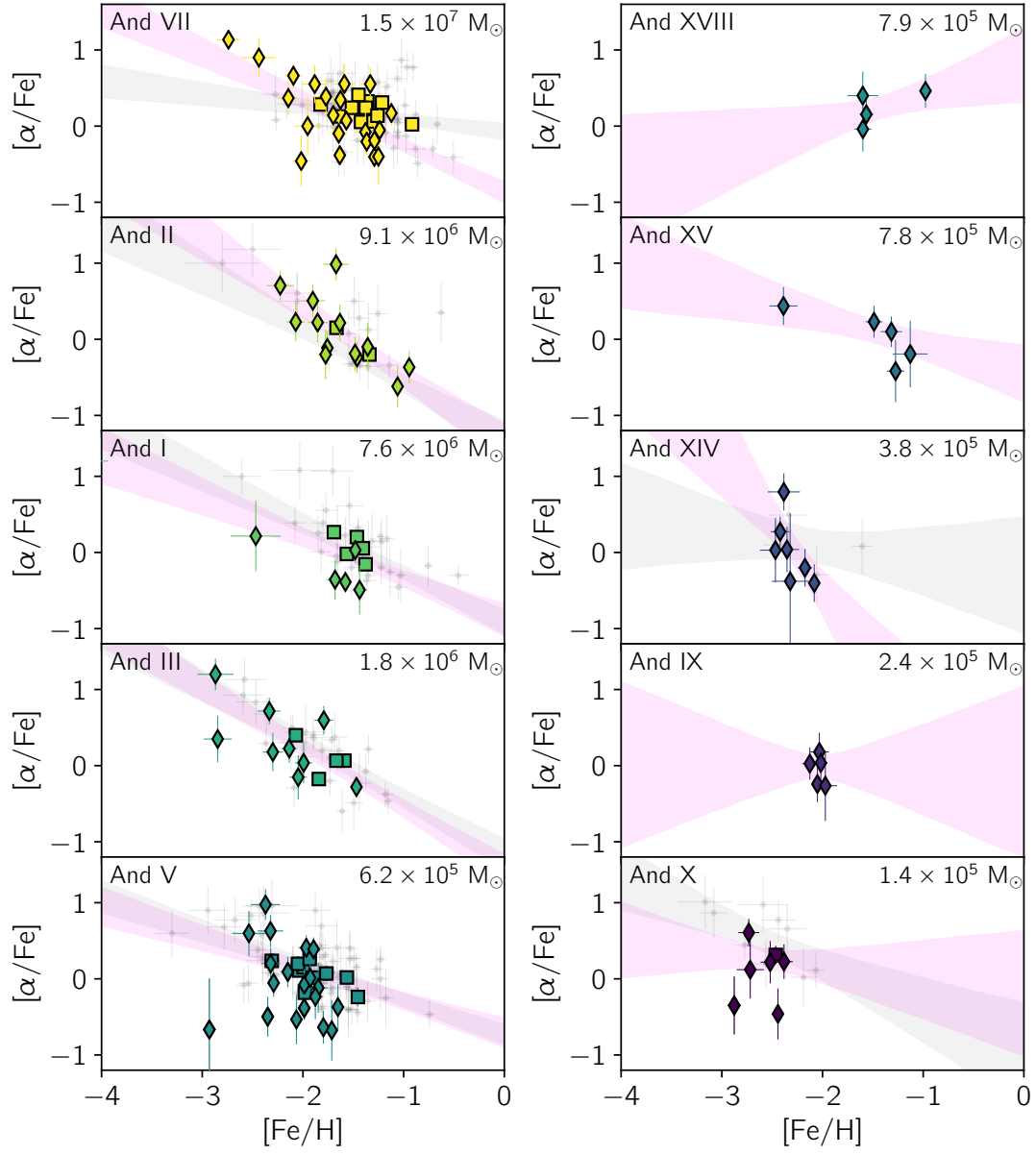**Figure 16.** The same as Figure 8, but for stars binned by T_{eff}.

Figure 17. The same as Figure 9, but for stars binned by T_{eff}.